

ACTION-BASED DYNAMICAL MODELLING FOR THE MILKY WAY DISK: THE INFLUENCE OF SPIRAL ARMS

WILMA H. TRICK^{1,2}, JO BOVY³, ELENA D'ONGHIA^{4,5}, AND HANS-WALTER RIX¹

Draft version September 7, 2016

ABSTRACT

RoadMapping is a well-tested dynamical modelling machinery developed to constrain the Milky Way's (MW) gravitational potential by simultaneously fitting an axisymmetric parametrized potential and action-based orbit distribution function (DF) to discrete 6D phase-space measurements of stars in the Galactic disk. In this work we demonstrate *RoadMapping*'s robustness in the presence of spiral arms by modelling data drawn from a N-body simulation snapshot of a MW-like spiral galaxy, exploring survey volumes with radii $500 \text{ pc} \leq r_{\max} \leq 5 \text{ kpc}$. The potential constraints are very robust, even when using the most simple action-based DF, the quasi-isothermal DF (qDF). The best-fit *RoadMapping* model always recovers the correct gravitational forces where most of the stars that entered the analysis are located. For data from large survey volumes *RoadMapping* finds axisymmetric models that average well over the spiral arms. Unsurprisingly, the models are slightly biased by the excess of stars in the spiral arms. Survey volumes with $r_{\max} \leq 3 \text{ kpc}$ give predictions for an overall axisymmetric potential as good as those from larger volumes. However, only for $r_{\max} = 5 \text{ kpc}$ is the correct halo scale length recovered. Potentials derived from small survey volumes ($r_{\max} < 2 \text{ kpc}$) centered on inter-arm regions can be more reliably extrapolated than those from small volumes affected by spiral arms. We discuss two possible applications of *RoadMapping* to the stellar phase-space measurements from the upcoming Gaia data releases: (i) finding an overall axisymmetric potential model for the MW from data covering a large volume, (ii) measuring non-axisymmetric structures in the MW's disk by modelling data in small volumes independently. [TO DO: Jo writes: "Need some sort of conclusion for these two."] [TO DO: HW suggests to replace the last sentence with "Our analysis implies that building axisymmetric models for Galaxy with upcoming Gaia data will lead to sensible and robust approximations of the Milky Way's potential."] [TO DO: How many words?]

Keywords: Galaxy: disk — Galaxy: fundamental parameters — Galaxy: kinematics and dynamics — Galaxy: structure — [TO DO]

1. INTRODUCTION

[TO DO: Make sure to change the text everywhere to "We are surprised that the qDF fits", to "at least for the overall axisymmetric average the qDF should be a good model, because of the initial disk setup. If we capture the spiral arms, we did not know beforehand."]

An important basis for learning more about the Milky Way's (MW) overall gravitational potential and orbit distribution function (DF)—which are crucial for understanding galaxy structure and formation (Rix & Bovy 2013) [TO DO: HW wants to remove this half-sentence]—is to find the “best possible” axisymmetric model for the Galaxy. Given such a model the identification and characterization of non-axisymmetries like the bar, spiral arms or stellar streams in stellar phase-space (and chemical abundance) data would then become more straightforward.

Several approaches to constrain an axisymmetric potential and/or orbit DF have recently been put forward: Bovy & Rix (2013) and Piffl et al. (2014) fitted potential and DF simultaneously to stellar kinematics in the disk and got precise constraints on the overall potential; Sanders & Binney (2015) and Das & Binney (2016) investigated extended DFs for the disk and halo respectively

(given a fiducial potential), that included in addition to the distribution in orbit space also the metallicity of each star.

In this work we will continue our investigation of the *RoadMapping* approach (“Recovery of the Orbit Action Distribution of Mono-Abundance Populations and Potential INference for our Galaxy”). The first application of *RoadMapping* was done by Bovy & Rix (2013) and Trick et al. (2016), hereafter Paper I, performed a detailed analysis of the strengths and limitations of the approach. *RoadMapping* presumes that simple stellar populations in the MW disk—be it mono-abundance populations (Bovy et al. 2012a,c,b, 2016) (i.e., stars with the same [Fe/H] and [α/Fe]) or maybe also mono-age populations (Bird et al. 2013; Martig et al. 2014, 2016; Minchev et al. 2014; Ness et al. 2016)—follow simple orbit DFs, like, e.g., the quasi-isothermal DF (qDF) by Binney & McMillan (2011) (Ting et al. 2013). The qDF is expressed in terms of the orbital actions $\mathbf{J} = (J_R, J_\phi = L_z, J_z)$, which are integrals of motion, quantify the amount of the orbit's oscillation in each of the coordinate directions (R, ϕ, z) and are therefore excellent orbit labels. Given an assumed gravitational potential one can calculate the orbital actions from the stars' current phase-space positions (\mathbf{x}, \mathbf{v}) (Binney 2012; Sanders & Binney 2016) [TO DO: Jo writes: "Bovy (2014) presents general method $(\mathbf{x}, \mathbf{v}) \rightarrow (\mathbf{J}, \boldsymbol{\theta})$."]. Only if the assumed gravitational potential is realistic, this stellar action distribution will follow a realistic orbit DF like the qDF [TO DO: Jo thinks the last half sentence is not very clear.]. This allows one to simultaneously fit potential and or-

¹ Max-Planck-Institut für Astronomie, Königstuhl 17, D-69117 Heidelberg, Germany

² Correspondence should be addressed to trick@mpia.de.

³ Department of Astronomy and Astrophysics, University of Toronto, 50 St. George Street, Toronto, ON, M5S 3H4, Canada

⁴ Department of Astronomy, University of Wisconsin, 2535 Sterling Hall, 475 N. Charter Street, Madison, WI 53076, USA

⁵ Alfred P. Sloan Fellow

bit DF to observations. [TO DO: HW writes about this paragraph: "Not clearly phrased. You get a well defined solution, whether the DF (or Phi) is 'realistic' or not."]

Bovy & Rix (2013) employed this approach to measure the Milky Way's surface density profile within 1.1 kpc using 43 MAPs in the Galactic disk from the SDSS/SEGUE survey (Yanny et al. 2009). Their potential model had only two free parameters (disk scale length and relative halo-to-disk contribution to the radial force at the solar radius). To account for missing model flexibility they constrained the surface density for each MAP only at one best radius. The profile they derived in this fashion had a scale length of $R_s = 2.5$ kpc and was—in the regime $R > 6.6$ kpc—later confirmed by Piffl et al. (2014) using a different action-based procedure.

Given the success of this first application and in anticipation of the upcoming data releases from Gaia in 2016–2022 (Eyer et al. 2013), Paper I improved the *RoadMapping* machinery and studied its strengths and breakdowns in detail, by investigating a large suite of mock data sets. Under the prerequisite of axisymmetric data and model, they found that *RoadMapping*'s modelling success is stable against minor misjudgements of DF or selection function, and that—if the true potential is not contained in the proposed family of model potentials—one can still find a good fit [TO DO: Jo wants me to add "that returns the correct forces" here.], given the limitations of the model. Paper I also found that measurement uncertainties of the order of those by the final Gaia data release should be good enough (within 3 kpc from the Sun) to allow for precise and unbiased modelling results.

The MW is, however, not axisymmetric. The bulge contains a strong bar (Liszt & Burton 1980; Blitz & Spergel 1991; Hammersley et al. 2000; Wegg & Gerhard 2013) and the disk itself is threaded by spiral arms (Oort et al. 1958; Georgelin & Georgelin 1976; Churchwell et al. 2009; Reid et al. 2014) [TO DO: More references] and (ring-like) overdensities (Newberg et al. 2002; Jurić et al. 2008; Xu et al. 2015), which induce non-circular motions and asymmetries in stellar number counts and correspond consequently to a non-axisymmetric gravitational potential and stellar DF. [TO DO: Jo writes: "Could also cite kinematic evidence: moving groups (Eggen (????), Dehnen (1998); Famaey et al. (2005); Bovy et al. (2009); Bovy & Hogg (2010)) and streaming motions (in 21 cm or velocities) (Bovy et al. 2015; Williams et al. 2013), Siebert et al. 2013 or 2014)" —> Ich finde das Eggen und Siebert paper nicht ...]

As *RoadMapping* and related approaches only can build axisymmetric models, this is an important breakdown of modelling assumptions which was not investigated in Paper I. In this paper we want to understand in which respects *RoadMapping* will still give reliable constraints on the MW's gravitational potential in the presence of spiral arms.

Our investigation makes use of a N-body simulation snapshot of a spiral galaxy with strong spiral arms (D'Onghia et al. 2013) to draw mock data in regions with different spiral arm strengths. We then apply the *RoadMapping* machinery to these data sets and test how well we recover the local and overall gravitational potential.

In Paper I we tested and confirmed separately the robustness of *RoadMapping* in the case that data came

from a different model family of either potential or DF than assumed in the dynamical modelling. What would happen if both potential and DF model families were slightly wrong at the same time? The set-up of this study will automatically cover this important test case: The disk potential and orbit DF models that we are using are partly chosen because of their simplicity and computational advantages and—in case of the qDF—because that's what we are planning to use in the MW. We did not have any indications that they might be especially well-suited to describe an axisymmetric version of this simulated galaxy—quite the contrary.

[TO DO: HW wants to know what the first and second aspects were...] Finally, in a non-axisymmetric potential, the three actions will not be strict integrals of motions. (Vera-Ciro & D'Onghia 2016) [TO DO: more references] [TO DO: Jo writes: "obvious?"].

Though non-axisymmetry could be a sever problem for *RoadMapping*, we show in this paper that *RoadMapping* potential estimates are still surprisingly accurate, which makes us optimistic that they will be also for the MW. [TO DO: Jo writes: "BR13 did not use in-plane motions to avoid spiral arm effects..."]

This paper is organized as follows. Section 2 describes the N-body simulation snapshot of a MW-like spiral galaxy, that we are going to model in this study, explains how we extract 6D stellar phase-space data from it, and how we quantify the spiral arm strength. Section 3 summarizes the *RoadMapping* dynamical modelling framework and introduces the DF and potential model that will fit to the data. Section 4 is dedicated to presenting the results: In Section 4.1 we discuss in detail the *RoadMapping* modelling results derived from a data set within a survey volume with radius $r_{\max} = 4$ kpc around the Sun. Section 4.2 investigates then a whole suite of *RoadMapping* analyses, corresponding to survey volumes of different sizes and different positions within the galaxy and with respect to the spiral arms. In Section 5 we discuss the results and conclude in Section 6.

[TO DO: Jo writes: "investigated here?" —> no idea what he means?]

2. DATA FROM A GALAXY SIMULATION

[TO DO: HW writes: "There is much detail, but not the basic reason why we use that simulation: it has enough particles... [to do ...]"]

2.1. Description of the galaxy simulation snapshot

In this work we use stellar phase-space data drawn from a high-resolution N-body simulation snapshot of a disk galaxy by D'Onghia et al. (2013) carried out with the GADGET-3 code and described in Springel et al. (2005) [TO DO: Jo writes: "not actually described there (Gadget ? is)" —> I can't read that.], in which overdensities with properties similar to giant molecular clouds induced prominent spiral arms—and therefore non-axisymmetric sub-structure—via the swing amplification mechanism. For details see D'Onghia et al. (2013), here we summarize the essential characteristics.

The simulation has a gravitationally evolving stellar disk within a static/rigid analytic dark matter halo.

The analytic halo follows a Hernquist (1990) profile

$$\rho_{\text{dm}}(r) = \frac{M_{\text{dm}}}{2\pi} \frac{a_{\text{dm}}}{r(r + a_{\text{dm}})^3} \quad (1)$$

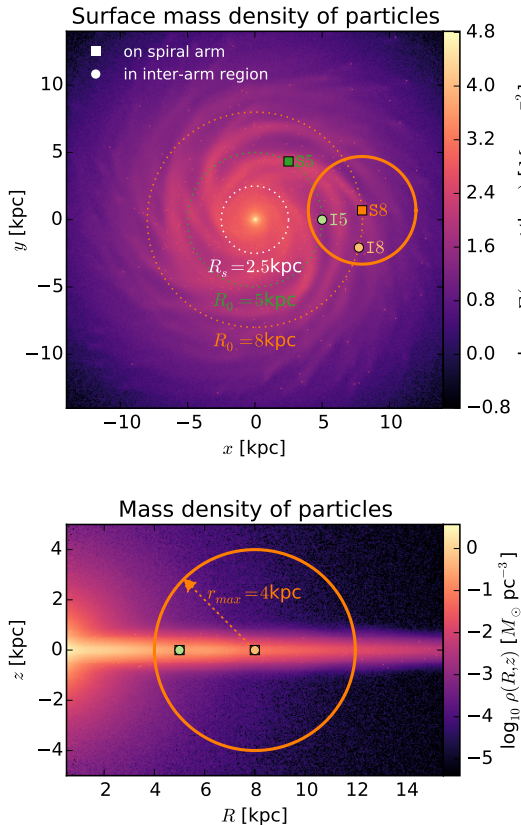


Figure 1. Simulation snapshot by D’Onghia et al. (2013). Shown are the surface mass density (in the (x, y) -plane, panel [TO DO]) and mass density (in the (R, z) -plane, panel [TO DO]) of the “star” particles belonging to disk, bulge and giant molecular clouds. (The dark matter halo in this simulation is static and analytic and not shown here.) Overplotted are the disk’s scale length $R_s = 2.5$ kpc (see Section 2.1) and the radii at which we center our test survey volumes in this investigation, $R_0 = 8$ kpc and $R_0 = 5$ kpc. The centers of the different survey volumes are marked with a square, if the survey volume is centered on a spiral arm (S8 and S5), or with a circle, if the volume is centered on an inter-arm region (I8 and I5). The orange circle with radius $r_{\max} = 4$ kpc marks the survey volume in which we conduct the analysis discussed in detail in Section 4.1. [TO DO: Make M_\odot not italic. Make two panels and no titles. Make labels in subscript rm.]

with total halo mass $M_{\text{dm}} = 9.5 \cdot 10^{11} M_\odot$ and scale length $a_{\text{dm}} = 29$ kpc (Elena D’Onghia, private communication).

The disk consists of 10^8 “disk star” particles, each having a mass of $\sim 370 M_\odot$, and 1000 “giant molecular cloud” particles with mass $\sim 9.5 \cdot 10^5 M_\odot$. Initially the particles are distributed following an exponential disk profile with density

$$\rho_*(R, z) = \frac{M_*}{4\pi z_0 R_s^2} \operatorname{sech}^2\left(\frac{z}{z_0}\right) \exp\left(-\frac{R}{R_s}\right), \quad (2)$$

with $R_s = 2.5$ kpc and $z_0 = 0.1 R_s$ and total disk mass $M_* = 0.04 \cdot M_{\text{dm}} = 3.8 \cdot 10^{10} M_\odot$.

The bulge consists of 10^7 “bulge star” particles with mass $\sim 950 M_\odot$ and they are distributed following a spherical Hernquist profile analogous to Equation (1), with total mass $M_{\text{bulge}} = 0.01 \cdot M_{\text{dm}} = 9.5 \cdot 10^9 M_\odot$ and scale length $a_{\text{bulge}} = 0.1 \cdot R_s = 0.25$ kpc.

The simulation snapshot which we are using in this work has evolved under its own gravity for ~ 250 Myr, which corresponds to approximately one orbital period

Table 1
Vantage points within the galaxy simulation snapshot around which we center survey volumes of radius r_{\max} .

name	position	R_0 [kpc]	ϕ_0 [degrees]	legend
S8	on spiral arm	8	5	■
I8	in inter-arm region	8	-15	○
S5	on spiral arm	5	60	■
I5	in inter-arm region	5	0	○

Note. — All volumes are centered on $z_0 = 0$ in the plane of the disk, and ϕ_0 is measured counter-clockwise from the positive x -coordinate axis.

at $R \sim 8$ kpc. The mass density of simulation particles (without the DM halo) at this snapshot time is shown in Figure 1. Pronounced spiral arms have developed due to the “molecular cloud perturbers”, which can be seen in Figure 1 as small overdensities in the disk. The spherical bulge and very flattened disk are shown in the lower panel in Figure 1.

We have confirmed that the gravitational center of the particles corresponds to the coordinate origin.

2.2. Survey volume and data

The selection function of all-sky surveys like Gaia, that are only limited by the brightness of the tracers, are contiguous and—when ignoring anisotropic effects like dust obscuration—spherical in shape. For simplicity we will use spherical survey volumes centered on different vantage points and with sharp edges at a radius r_{\max} around it (see also Section 3.1), which corresponds to a magnitude cut for stellar tracers all having the same luminosity.

Figure 1 illustrates the different survey volume positions we use in this study: We use each a volume with $r_{\max} = 1, 2, 3, 4$ or 5 kpc centered on a spiral arm and on an inter-arm region at both the equivalent of the solar radius in this simulation, $R = 8$ kpc, and at $R = 5$ kpc, where the spiral arms are more pronounced (see Figure 2) than at $R = 8$ kpc. The exact positions of the vantage points are summarized in Table 1.

From each volume we draw $N_* = 20,000$ random “disk star” particles from the simulation and use their phase-space positions $(\mathbf{x}_i, \mathbf{v}_i)$ within the simulated galaxy’s restframe as data.

To make the data sample more realistic, one would actually have to add measurement uncertainties, especially to the distances from the survey volume’s central vantage point and the proper motions measured from there. We decided not to include measurement uncertainties: Firstly, their effect on *RoadMapping* modelling has been already investigated in Paper I and we found that the measurement uncertainties of the last data release of Gaia should be small enough to not disturb the modelling to much. Secondly, in this study we want to isolate and investigate the deviations of the data from the assumed potential and DF model and axisymmetry independently of other effects.

2.3. Symmetrized potential model

For a galaxy with pronounced spiral arms an axisymmetric model matter distribution can per se not reproduce the true matter distribution globally. We derived an *overall best fit symmetrized* potential model from the distribution of particles to be able (i) to quantify the non-axisymmetries in the simulation snapshot better and (ii)

Table 2
Best fit parameters of the DEHH-Pot (see Section 2.3), which we use as the global best fit symmetrized potential model.

circular velocity	$v_{\text{circ}}(R_\odot)$	222 km s ⁻¹
disk scale length	h_r	2.5 kpc
disk scale height	h_z	0.17 kpc
halo fraction	f_{halo}	0.54
halo scale length	a_{halo}	29 kpc
bulge mass	M_{bulge}	$0.95 \cdot 10^{10} M_\odot$
bulge scale length	a_{bulge}	0.25 kpc

Note. — The halo fraction, f_{halo} , and circular velocity at the Sun, $v_{\text{circ}}(R_\odot)$, which scales the total mass of the model, are defined in Equations (22) and (23).

to compare how close our axisymmetric *RoadMapping* results can get to it.

We derive this model by fitting axisymmetric analytical functions to the density distribution of each of the galaxy component's particles: The bulge and halo follow each a Hernquist profile by construction (see Section 2.1). The disk with its spiral arms however does deviate strongly from its initial conditions in Equation (2). We chose a double exponential disk model to fit the particle distribution in the disk. The best fit parameters for this reference potential, to which we will refer as the **DEHH-Potential** (Double-Exponential disk + Hernquist halo + Hernquist bulge) in the remainder of this work, are given in Table 2. As can be seen in Figures 4 and 5 in Section 4.1 below, the DEHH-Pot fits the overall density distribution very well. Its density profile might be a little stepper around $z \sim 0$ than the actual particle distribution, but this should not affect the overall discussion, as the radial density, surface density and disk-to-halo ratio profiles are so well reproduced.

2.4. Quantifying the strength of spiral arms

Depending on size and position of the survey volume the spiral arms and inter-arm regions dominate the stellar distribution within the survey volume to different degrees. To quantify the strength of the spiral arm, we introduce the quantity

$$\Delta_{\text{Spiral}}(x_k, y_k) \equiv \frac{\Sigma_{\text{disk},T}(x_k, y_k \mid |z| \leq 1.5 \text{ kpc})}{\Sigma_{\text{disk},S}(x_k, y_k \mid |z| \leq 1.5 \text{ kpc})} - 1 \quad (3)$$

where $\Sigma_{\text{disk},\alpha}$ is the surface density of the disk component of the simulation snapshot ($\alpha = T$) [TO DO: HW writes: "What does that mean?"] or of the symmetrized snapshot model DEHH-Pot in Section 2.3 ($\alpha = S$) within the survey volume,

$$\Sigma_{\text{disk},\alpha} \equiv \int_{-1.5 \text{ kpc}}^{1.5 \text{ kpc}} \rho_{\text{disk},\alpha}(x_k, y_k, z) \, dz. \quad (4)$$

(x_k, y_k) is the centroid of a surface area element $(x_k \pm \delta, y_k \pm \delta)$ with $\delta = 0.25 \text{ kpc}$. $(x_c = R_{0,c} \times \cos \phi_{0,c}, y_c = R_{0,c} \times \sin \phi_{0,c}, z_c = 0)$ is the position of the survey volume's center within the simulation, with $c \in \{\text{S8, I8, S5, I5}\}$ and $(R_{c,0}, \phi_{c,0})$ given in Table 1. We consider all $n \simeq \pi r_{\max}^2 / 4\delta^2$ values of $\Delta_{\text{Spiral}}(x_k, y_k)$ inside a given survey volume of radius r_{\max} around position c and

calculate the mean and standard deviation,

$$\begin{aligned} \langle \Delta_{\text{Spiral}} \rangle &\equiv \langle \Delta_{\text{Spiral}}(r \leq r_{\max} \mid c) \rangle \\ &\equiv \frac{1}{n} \sum_{j=1}^n \Delta_{\text{Spiral}}(x_k, y_k) \end{aligned} \quad (5)$$

$$\begin{aligned} \sigma_{\Delta_{\text{Spiral}}} &\equiv \sigma[\Delta_{\text{Spiral}}(r \leq r_{\max} \mid c)] \\ &\equiv \sqrt{\frac{1}{n} \sum_{j=1}^n n [\Delta_{\text{Spiral}}(x_k, y_k) - \langle \Delta_{\text{Spiral}} \rangle]^2} \end{aligned} \quad (6)$$

$$\text{with } (x_k - x_c)^2 + (y_k - y_c)^2 \leq r_{\max}. \quad (7)$$

This gives us information if a spiral arm or an inter-arm region dominates the survey volume ($\langle \Delta_{\text{Spiral}} \rangle > 0$ for spiral arms, $\langle \Delta_{\text{Spiral}} \rangle < 0$ for inter-arm regions) and how large the relative contrast between spiral arms and inter-arm regions is ($\sigma_{\Delta_{\text{Spiral}}}$). For example, small volumes sitting completely within an inter-arm region, or large volumes that contain—in addition to some spiral arms and depleted inter-arm regions—also large areas of unperturbed disk, will have an overall small relative spiral contrast $\sigma_{\Delta_{\text{Spiral}}}$.

3. ROADMAPPING MODELLING

[TO DO: Jo writes: "Refer to paper I for full details!"
→ Also, I should write an intro sentence here.]
[TO DO: HW writes: "Is that not near identical to Paper I – MUCH shorter?"]

3.1. Likelihood

The data that goes into the modelling are the 6D position and velocity coordinates $(\mathbf{x}_i, \mathbf{v}_i)$ of N_* stars within the survey volume. For simplicity we use a purely spatial selection function $\text{SF}(\mathbf{x})$ of spherical shape,

$$\text{SF}(\mathbf{x}) \equiv \begin{cases} 1 & \text{if } |\mathbf{x} - \mathbf{x}_0| \leq r_{\max} \\ 0 & \text{otherwise} \end{cases}, \quad (8)$$

whose maximum radius r_{\max} defines the boundary of the survey volume, and which is centered on $\mathbf{x}_0 \equiv (R_0, \phi_0, z_0 = 0)$. Given a parametrized potential model $\Phi(R, z)$ with parameters p_Φ , the i -th star is on an orbit characterized by the orbital actions

$$\mathbf{J}_i \equiv \mathbf{J}[\mathbf{x}_i, \mathbf{v}_i \mid p_\Phi]. \quad (9)$$

The probability of stars to be on the orbit \mathbf{J}_i is proportional to a given orbit distribution function $\text{DF}(\mathbf{J})$ with parameters p_{DF} ,

$$\begin{aligned} \text{DF}(\mathbf{J}_i \mid p_{\text{DF}}) &\equiv \text{DF}(\mathbf{J}[\mathbf{x}_i, \mathbf{v}_i \mid p_\Phi] \mid p_{\text{DF}}) \\ &\equiv \text{DF}(\mathbf{x}_i, \mathbf{v}_i \mid p_\Phi, p_{\text{DF}}), \end{aligned} \quad (10)$$

where the latter equivalence arises from the Jacobian determinant between the angle-action coordinates $(\boldsymbol{\theta}, \mathbf{J})$ and cartesian phase-space coordinates (\mathbf{x}, \mathbf{v}) , which is $|\partial(\mathbf{x}, \mathbf{v})/\partial(\boldsymbol{\theta}, \mathbf{J})| = 1$ and therefore allows us to treat the DF equivalently as a distribution of current phase-space coordinates or a distribution of orbital actions only, with uniform distribution in the angles $\boldsymbol{\theta}$. In some sense, the $\text{DF}(\mathbf{J})$ describes what we expect a realistic phase-mixed stellar population in the MW disk to look like.

The joint likelihood of the i -th star being on an orbit \mathbf{J} in the potential Φ and being within the survey volume

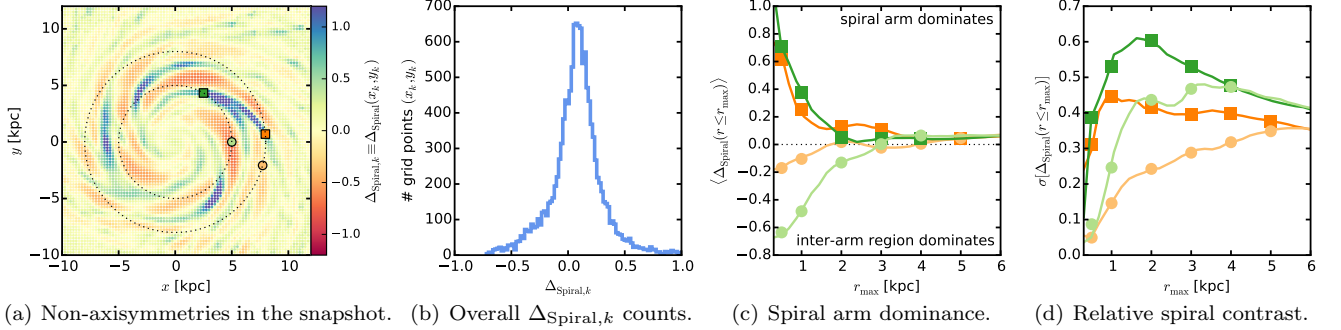


Figure 2. Contrast and dominance of the spiral arms. Panel 2(a) shows the local spiral strength $\Delta_{\text{Spiral},k}$ (calculated according to Equation (3) as described in Section 2.4) at regular grid points (x_k, y_k) with bin width 0.25 kpc. Marked are the centroids of the four test survey volumes of this study analogous to Figure 1. The panels 2(b) and 2(d) then show the dominance and relative contrast of spiral arms and inter-arm regions within each survey volume, depending on the volumes' size, r_{\max} , and position (colour-coded according to panel 2(a)). As measure for the spiral dominance we use the mean $\langle \Delta_{\text{Spiral}}(r \leq r_{\max}) \rangle$, and for the relative spiral contrast the standard deviation $\sigma[\Delta_{\text{Spiral}}(r \leq r_{\max})]$, calculated on the basis of all Δ_{Spiral} measurements within the given survey volume. We chose two volumes in which the spiral arms dominate, and two in which an inter-arm region dominates. The dominance and contrast of spiral arms and inter-arm regions is stronger at $R = 5$ kpc than at $R = 8$ kpc. Also, inter-arm regions appear larger and smoother than spiral arms, as already inside a small volume centred on a spiral arm the contrast is quite large. The larger the volume the more does the overall effect of spiral arms and inter-arm regions average out. [TO DO: Jo suggested to look into implementing a sech² disk for galpy to not have the slight bias in mean(κ) at higher rmax. Maybe it's easy to implement. Maybe it isn't.] [TO DO: HW on the first panel: "Why not make this panel the 2nd panel of Fig 1?"] [TO DO: Include legend with survey volume names.]

is therefore

$$\mathcal{L}_i \equiv \mathcal{L}(\mathbf{x}_i, \mathbf{v}_i) = \frac{\text{DF}(\mathbf{x}_i, \mathbf{v}_i | p_\Phi, p_{\text{DF}}) \cdot \text{SF}(\mathbf{x}_i)}{\int \text{DF}(\mathbf{x}, \mathbf{v} | p_\Phi, p_{\text{DF}}) \cdot \text{SF}(\mathbf{x}) d^3x d^3v}. \quad (11)$$

The details how we evaluate the likelihood normalisation numerically to sufficiently high enough precision are discussed in Paper I.⁶

In the scenario considered in this paper it can happen that there are a few (~ 1 in 20,000) stars entering the catalogue that are for some reason on rather extreme orbits, e.g., moving radially directly towards the center. These kinds of orbits do not belong to the set of orbits that we classically expect to make up a overall smooth galactic disk. To avoid that such single stars with very low likelihood have a strong impact on the modelling we introduce here a simple outlier model,

$$\mathcal{L}_i \rightarrow \max(\mathcal{L}_i, \epsilon \cdot \text{median}(\mathcal{L})), \quad (12)$$

where $\epsilon = 0.001$ for $N_* = 20,000$ stars and $\text{median}(\mathcal{L})$ is the median of all the N_* stellar likelihoods \mathcal{L}_i with the given p_Φ and p_{DF} . This outlier model was not used in Paper I.

[TO DO: Jo writes: "This is a strange outlier model! Realistically a broad Gaussian in v and flat in x might be better." — Yes, might be. But HW suggested this, and now it's to late anyway...]

Following Paper I, we assume for now uninformative flat priors on the model parameters p_Φ and p_{DF} and find the maximum and width of the posterior probability function

$$\text{pdf}(p_\Phi, p_{\text{DF}} | \text{data}) \propto \prod_{i=1}^{N_*} \mathcal{L}_i \cdot \text{prior}(p_\Phi, p_{\text{DF}}) \quad (13)$$

⁶ In the terminology of Paper I we use the high numerical accuracy $N_x = 20$, $N_v = 28$, $n_\sigma = 5.5$ to calculate the likelihood normalisation, or in other words, to evaluate the spatial and velocity integrals over the qDF within the survey volume. For the action interpolation grid following Bovy (2015), we use $R_{\max} = 40$ kpc, $n_E = 70$, $n_\psi = 40$, $n_{L_z} = 50$ in their terminology.

using a nested-grid approach and then explore the full shape of the *pdf* using a Monte Carlo Markov Chain (MCMC)⁷. Full details on this procedure are given in Paper I. [TO DO: Jo writes: "Also, don't think you've mentioned galpy yet."]

3.2. Distribution function model

The most simple action-based orbit distribution function exhibiting a disk-like structure may be the quasi-isothermal distribution function (qDF) introduced by Binney (2010) and Binney & McMillan (2011). It has proven to be a successful model to describe the orbit distribution of individual mono-abundance populations (MAPs) in the Galactic disk (Bovy & Rix 2013; Ting et al. 2013), that seem to be isothermal in z -direction (i.e., "quasi-isothermal"). Modelling approaches trying to capture the overall disk distribution (Piffl et al. 2014; Sanders & Binney 2015) were describing the Galactic disk as a superposition of many qDFs. The qDF, which we already used in Paper I, has the functional form

$$\begin{aligned} \text{qDF}(\mathbf{J} | p_{\text{DF}}) \\ = f_{\sigma_R}(J_R, L_z | p_{\text{DF}}) \times f_{\sigma_z}(J_z, L_z | p_{\text{DF}}) \end{aligned} \quad (14)$$

where

$$\begin{aligned} f_{\sigma_R}(J_R, L_z | p_{\text{DF}}) = n \times \frac{\Omega}{\pi \sigma_R^2(R_g) \kappa} \exp\left(-\frac{\kappa J_R}{\sigma_R^2(R_g)}\right) \\ \times [1 + \tanh(L_z/L_0)] \end{aligned} \quad (15)$$

$$f_{\sigma_z}(J_z, L_z | p_{\text{DF}}) = \frac{\nu}{2\pi \sigma_z^2(R_g)} \exp\left(-\frac{\nu J_z}{\sigma_z^2(R_g)}\right) \quad (16)$$

(Binney & McMillan 2011). The guiding-center radius R_g , circular frequency Ω , radial/epicycle frequency κ and vertical frequency ν describe the near-circular orbit with given angular momentum L_z in a given potential.

⁷ We use the MCMC software *emcee* by Foreman-Mackey et al. (2013).

Table 3
Best fit MNHH-Pot and qDF parameters as recovered from the *RoadMapping* analysis of a survey volume with $r_{\max} = 4$ kpc centered on a spiral arm at $R_0 = 8$ kpc (position S8).

circular velocity	$v_{\text{circ}}(R_\odot)$	$(223.0 \pm 0.1) \text{ km s}^{-1}$
Miyamoto-Nagai disk scale length	a_{disk}	$(3.62^{+0.06}_{-0.05}) \text{ kpc}$
Miyamoto-Nagai disk scale height	b_{disk}	$(0.26 \pm 0.02) \text{ kpc}$
halo fraction	f_{halo}	(0.53 ± 0.02)
halo scale length	a_{halo}	$(21 \pm 2) \text{ kpc}$
bulge mass	M_{bulge}	$0.95 \cdot 10^{10} M_\odot$ (fixed)
bulge scale length	a_{bulge}	0.25 kpc (fixed)
qDF tracer scale length	h_R	$(3.34^{+0.05}_{-0.04}) \text{ kpc}$
qDF radial velocity dispersion	$\sigma_{R,0}$	$(15.91 \pm 0.08) \text{ km s}^{-1}$
qDF vertical velocity dispersion	$\sigma_{z,0}$	$(14.0^{+0.2}_{-0.1}) \text{ km s}^{-1}$
qDF radial velocity dispersion scale length	$h_{\sigma,R}$	$(4.6 \pm 0.5) \text{ kpc}$
qDF vertical velocity dispersion scale length	$h_{\sigma,z}$	$(5.65^{+0.06}_{-0.07}) \text{ kpc}$

Note. — The bulge mass and scale length were fixed in the analysis to their true values, see Sections 2.1 and 3.3.

Counter-rotating orbits with $L_z < L_0$ are suppressed by the term $[1 + \tanh(L_z/L_0)]$ (with $L_0 \sim 10 \text{ km s}^{-1} \text{ kpc}$). We set the radial stellar tracer density $n(R_g)$ and velocity dispersion profiles $\sigma_z(R_g)$ and $\sigma_R(R_g)$ to

$$n(R_g | p_{\text{PDF}}) \propto \exp\left(-\frac{R_g}{h_R}\right) \quad (17)$$

$$\sigma_R(R_g | p_{\text{PDF}}) = \sigma_{R,0} \times \exp\left(-\frac{R_g - R_\odot}{h_{\sigma,R}}\right) \quad (18)$$

$$\sigma_z(R_g | p_{\text{PDF}}) = \sigma_{z,0} \times \exp\left(-\frac{R_g - R_\odot}{h_{\sigma,z}}\right). \quad (19)$$

The free model parameters of the qDF are therefore

$$p_{\text{PDF}} \equiv \{\ln h_R, \ln \sigma_{R,0}, \ln \sigma_{z,0}, h_{\sigma,R}, h_{\sigma,z}\}. \quad (20)$$

We do not have any stellar abundance or age information in the simulation snapshot we are going to investigate in this work, and we therefore cannot define stellar sub-populations. However, the disk of the galaxy simulation was originally set up as a single axisymmetric flattened particle population whose density decreases exponentially with radius (see Section 2.1). This is actually very similar to the stellar distribution generated by a single qDF, and motivates us therefore to use a single qDF to model the whole disk.

Locally, the *current* particle distribution in the snapshot at hand might be dominated by non-axisymmetries which evolved later in the simulation. We have no indication if for small survey volumes the qDF is still a good model for the data. We will use it anyway—to see how far we can get with the simplest possible model.

3.3. Potential model

In all *RoadMapping* analyses in this work we will fit an axisymmetric gravitational potential model to the data consisting of a (fixed and known) Hernquist bulge, a free Hernquist halo and a free Miyamoto-Nagai disk (Miyamoto & Nagai 1975),

$$\Phi_{\text{disk}}(R, z) = -\frac{GM}{\sqrt{R^2 + (a_{\text{disk}} + \sqrt{z^2 + b_{\text{disk}}^2})^2}}, \quad (21)$$

where a_{disk} and b_{disk} are the equivalents of a disk scale length and scale height. To use Hernquist profiles for halo

and bulge is motivated by our knowledge of the snapshot galaxy, and we fix the bulge's total mass and scale length to the true values (see Section 2.1 and Table 3). As the bulge contribution to the total radial force at $R_\odot = 8$ kpc is only $\sim 9 - 10\%$, this will not give the modelling an “unfair advantage”. The free model parameters of the halo are the halo scale length a_{halo} and the halo fraction, i.e., the relative halo-to-disk contribution to the radial force at the solar radius, defined as

$$f_{\text{halo}} \equiv \frac{F_{\text{R,halo}}}{F_{\text{R,disk}} + F_{\text{R,halo}}} \Big|_{\substack{R=R_\odot \\ z=0}}. \quad (22)$$

As parameter that scales the total mass of the galaxy model we use the circular velocity at the “solar” radius,

$$v_{\text{circ}}(R_\odot = 8 \text{ kpc}) \equiv \sqrt{R \frac{\partial \Phi}{\partial R}} \Big|_{\substack{R=R_\odot \\ z=0}}. \quad (23)$$

The total set of free potential model parameters is therefore

$$p_\Phi \equiv \{v_{\text{circ}}(R_\odot), a_{\text{disk}}, b_{\text{disk}}, a_{\text{halo}}, f_{\text{halo}}\}. \quad (24)$$

We will call this potential model the MNHH-Pot (Miyamoto-Nagai disk + Hernquist halo + Hernquist bulge) in the remainder of this work.

To estimate the stellar actions $\mathbf{J} = (J_R, L_z, J_z)$ in the axisymmetric MNHH-Pot, we are using the *Stäckel fudge* algorithm by Binney (2012), which is the best compromise between speed and accuracy and especially well-suited for action estimations in a thin disk (see Sanders & Binney 2016). To speed up the code even more, we also interpolate the actions on a grid (Binney 2012; Bovy 2015) and used a fixed Stäckel focal length of $\Delta = 0.45$ for the *Stäckel fudge*. We made sure, that the accuracy of the parameter estimates are not degraded by interpolation errors.

For the potential models and the qDF, as well as the *Stäckel fudge*, *RoadMapping* makes extensive use of the *galpy* python library by Bovy (2015)⁸.

The DEHH-Pot introduced in Section 2.3 with its double-exponential disk profile is better than the Miyamoto-Nagai disk in reproducing the overall radial

⁸ The *galpy* python package by Bovy (2015) can be downloaded from <http://github.com/jobovy/galpy>.

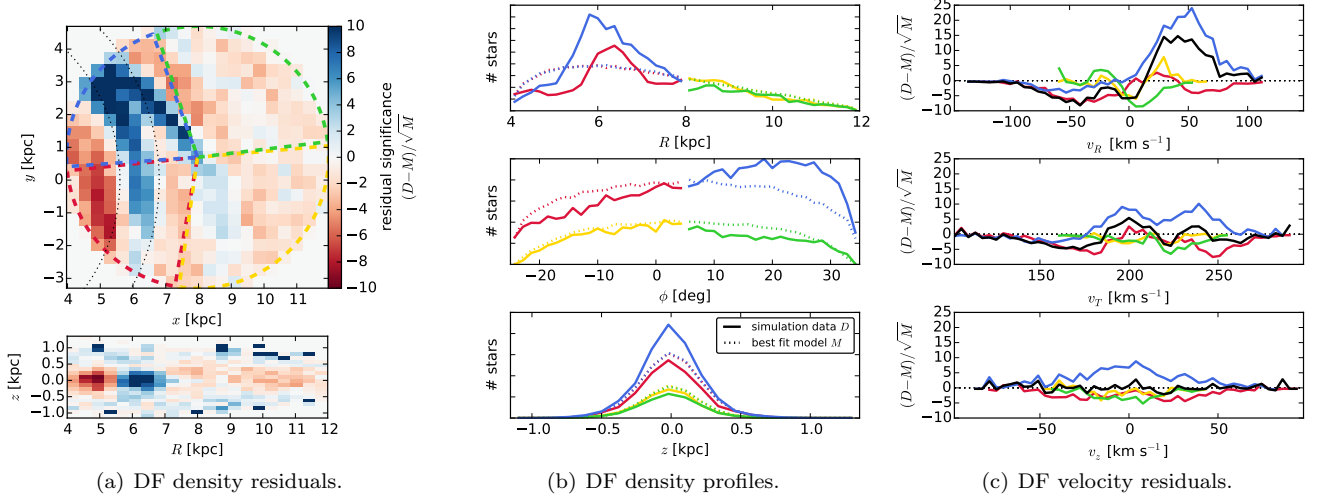


Figure 3. Comparison of the true and best fit stellar DF(\mathbf{x}, \mathbf{v}) in position-velocity space. The true DF(\mathbf{x}, \mathbf{v}) (i.e., the data D) is the distribution of all the stars in the data set drawn from the simulation snapshot (with $N_* = 20,000$ and $r_{\max} = 4$ kpc centered on position S8). The best fit DF(\mathbf{x}, \mathbf{v}) (i.e., the model M) is generated by MC sampling of the best fit qDF(J) in the best fit potential model from *RoadMapping* in Table 3, given the known selection function. Panel 3(a) shows the spatial density residual significance $(D - M)/\sqrt{M}$ of the projection to the (x, y) and (R, z) plane. (The MC sampled M is the expected number of stars per bin, and \sqrt{M} the expected error due to Poisson statistics.) In the (x, y) panel the following regions are marked: $R < 8$ kpc, $\phi > 5^\circ$ (blue), $R < 8$ kpc, $\phi < 5^\circ$ (red), $R > 8$ kpc, $\phi > 5^\circ$ (green), $R > 8$ kpc, $\phi < 5^\circ$ (yellow). Panels 3(b) and 3(c) show the density profiles and velocity residual significance along each of the 6D phase-space coordinates separately for each of the four spatial regions. The blue region is very much dominated by the non-axisymmetric spiral arm. For the yellow region the axisymmetric single-qDF model is a good description. Overall the qDF is a good average axisymmetric model for the data. (In panel 3(a) we overplot the radii $R_{\text{spiral}} \in [5.6, 6.8]$ kpc as black dotted lines to mark the approximate extent of the stronger spiral arm, to compare it with Figure 7.) [TO DO: Move legend to R panel and make it bigger] [TO DO: Jo writes: "I don't like boxes around legends"] [TO DO: Jo writes: "What is the black line?" — Add legend to panel (c).]

density slope, as we will see in Figures 4 and 5 in the next section, and which is also suggested by the initial disk configuration in Equation (2). However, the closed form expression of the potential in Equation (21) has the crucial advantage of allowing very fast force and therefore action calculations in *RoadMapping* modelling. And the gain in computational speed as compared to using the DEHH-Pot, which requires the evaluation of integrals and Bessel functions to calculate the forces, is essential. In addition, by using a potential model where we already know that it is not be the optimal model for the galaxy's disk, we challenge *RoadMapping* even further.

How should one compare the *RoadMapping* results for the best-fit MNHH-Pot with the fixed DEHH-Pot (Table 2) in the remainder of this work? When considering a *global* best fit potential model for the galaxy, *RoadMapping* model can not be better than the DEHH-Pot, which is therefore a global upper limit for *RoadMapping*'s modelling success. We note that in deriving the DEHH-Pot in Section 2.3 we used the correct decomposition into bulge, disk and halo components. *RoadMapping* however is only sensitive to the composite gravitational effect of the potential. Given the flexibility of the MNHH-Pot model used in *RoadMapping* and the restriction of the modelling to a survey volume, it could be possible that *RoadMapping* can do better in fitting the local potential inside the survey volume at the price of recovering the global potential parameters to less accuracy. We will discuss this in the following sections.

4. RESULTS

At the core of this work is a suite of 22 data sets consisting of the phase-space coordinates of stellar tracer particles, drawn from the spiral galaxy simulation snap-

shot introduced in Section 2.1. Each data set comes from a different survey volume within the galaxy's disk (see Section 2.2). We modelled all data sets with *RoadMapping* as described in Section 3, by fitting to it a single qDF (see Section 3.2) and the potential model MNHH-Pot (introduced in Section 3.3), comprised of a Miyamoto-Nagai disk, a Hernquist halo and a (fixed) Hernquist bulge. This resulted in 22 independent measurements of the simulated galaxy's potential and DF.

We present our results in two steps. In Section 4.1 we discuss all aspects of one of these *RoadMapping* models in detail. In Section 4.2 we then compare all 22 *RoadMapping* results, and discuss their differences in the context of spiral arms of different strength crossing the respective survey volumes.

4.1. An axisymmetric galaxy model from *RoadMapping*

We will focus in this section on one single data set for which we discuss all the different aspects of a *RoadMapping* model. This data set has $N_* = 20,000$ stars that were drawn from the spherical volume with $r_{\max} = 4$ kpc centered on a spiral arm at the "solar" radius $R_0 = 8$ kpc shown as orange sphere in Figure 1 (position S8). We chose this volume because of its position centred on a smaller spiral arm—similar to our Sun being located in the Orion spiral arm—and because it probes the galaxy's potential over an extended region. Our goal is to investigate the ability of this best fit *RoadMapping* model to serve as an overall axisymmetric model for the galaxy.

The parameters of the best fit MNHH-Pot and qDF recovered with *RoadMapping* from this data set are summarized in Table 3. The circular velocity $v_{\text{circ}}(R_\odot)$ and halo fraction f_{halo} are especially well recovered (compare to Table 2).

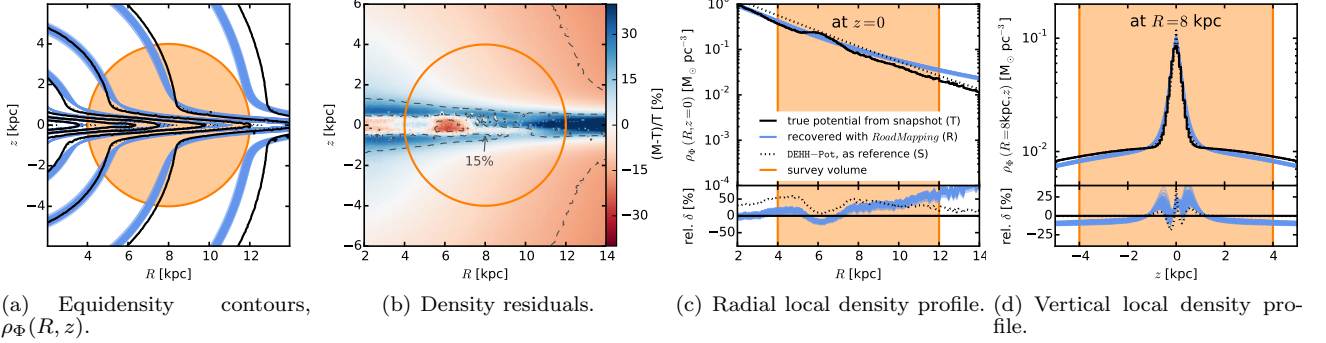


Figure 4. Comparison of the true and recovered overall matter density distribution ρ_Φ , generating the gravitational potential Φ . $\rho_{\Phi,T}$ is the true potential in the galaxy simulation snapshot (solid black line, averaged over the whole galaxy, $\Delta\phi = 2\pi$). $\rho_{\Phi,R}$ is the axisymmetric density distribution generated by the best fit MNHH-Pot recovered with *RoadMapping* (blue lines; 100 MC samples drawn from best fit *pdf*) from $N_* = 20,000$ stars in the survey volume S8 with $r_{\max} = 4$ kpc (orange). Panel 4(a) displays equidensity contours in the (R, z) plane. Overplotted is, as reference, also the overall axisymmetric DEHH-Pot's $\rho_{\Phi,S}$ (dotted black line; see Section 2.3). Panel 4(b) shows the relative difference between the true $\rho_{\Phi,T}$ and $\rho_{\Phi,M}$, where the latter is the recovered median *RoadMapping* model in Table 3. Over wide areas even outside of the survey volume the relative difference is less than 15%. Panels 4(c) and 4(d) show cuts through the density distribution along $(R, z = 0)$ and $(R = 8$ kpc, $z)$, and the relative residuals with respect to the true model, i.e., $\text{rel. } \delta \equiv (\rho_{\Phi,R} - \rho_{\Phi,T})/\rho_{\Phi,T}$. At $R \gtrsim 8$ kpc and $z \sim 0$ it becomes apparent that the chosen potential model cannot perfectly capture the structure of the disk. However, in the plane of the disk and at smaller radii within the survey volume, where most of the stars are located, the model gives good constraints on the density.

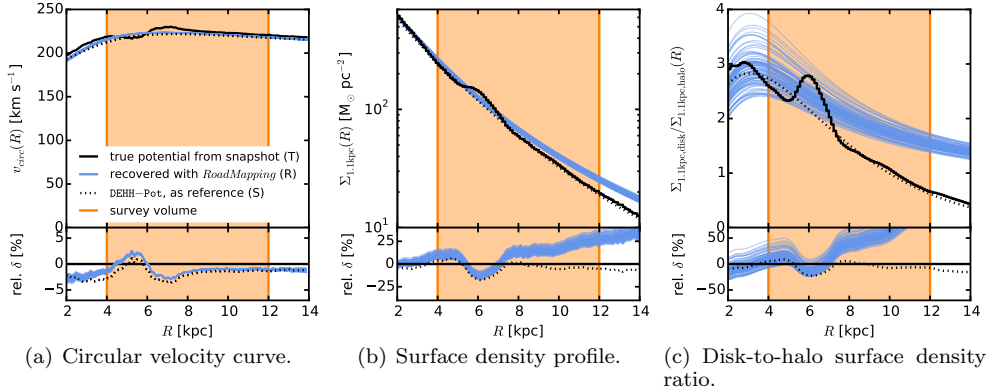


Figure 5. Comparison of the true and recovered circular velocity curve, $v_{\text{circ}}(R)$, surface density profile within $|z| \leq 1.1$ kpc, $\Sigma_{1.1\text{kpc}}(R)$, and disk-to-halo ratio of the surface density along R , $\Sigma_{1.1\text{kpc,disk}}/\Sigma_{1.1\text{kpc,halo}}(R)$, generated by the potential Φ . We show this for the true potential of the galaxy simulation snapshot (solid black line for the global average over $\phi_0 \pm \pi$) and the axisymmetric model potential recovered with *RoadMapping* (solid blue lines; 100 MC samples drawn from the *pdf*; see Table 3). Overplotted are also the profiles of the symmetrized “true” DEHH-Pot (dotted black line; see Section 2.3 and Table 2). The circular velocity curve is recovered to less than 5%, especially at larger radii. For the surface density and disk-to-halo ratio *RoadMapping* recovers the truth at radii $\lesssim 7$ kpc. The deviations at larger radii are connected to the discrepancies in the density in Figure 4. [TO DO: Make index circ rm]

4.1.1. Recovering the stellar distribution

The *RoadMapping* fit itself takes place in action space. However, an important sanity check to decide if the fit was successful, is to test if the best fit *RoadMapping* model (i.e., best fit action-based DF in best fit potential and in given selection function) generates a stellar distribution that reproduces the distribution of data points in the phase-space of observables, (\mathbf{x}, \mathbf{v}) . This comparison is shown in Figure 3. We note that the spiral arms introduce very strong non-axisymmetries in the data, both in the spatial and the velocity distribution (especially in v_R , where a lot more stars move outward than inward as compared to an axisymmetric model). We therefore compare the data and fit separately for different spatial regions, $R > 8$ kpc and $R < 8$ kpc, and $\phi < 5^\circ$ and $\phi > 5^\circ$. In the region where the spiral arm dominates (blue in Figure 3) the best fit *RoadMapping* model is actually a very poor model. However, what the model underestimates

in the spiral arm, it slightly overestimates in the other regions and is therefore indeed something like a good average model for the overall distribution. Especially the region at $R > 8$ kpc and $\phi < 5^\circ$ (yellow in Figure 3), where neither the spiral arm nor the inter-arm regions dominate strongly, is very well described by the model. We already expected the qDF to be a plausible model for the unperturbed disk. Here, we explicitly show that this is indeed the case, which very encouraging! The only exception are of course the spiral arms, which the qDF had no chance to begin with.

4.1.2. Recovering the gravitational potential

As shown in the previous section the best fit *RoadMapping* model seems to reproduce the stellar phase-space distribution quite well. But is the corresponding potential close to the true potential?

Figures 4 and 5 compare the true potential from the

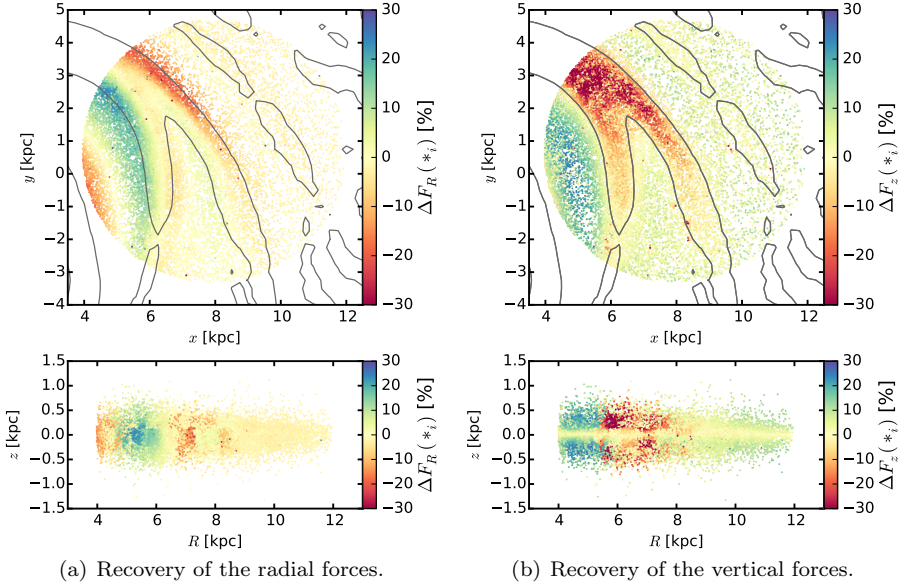


Figure 6. Recovery of the gravitational forces with *RoadMapping*. We compare the true gravitational forces with the forces estimated from the *RoadMapping* best fit potential in Table 3 at the (x, y) positions (upper panels) and (R, z) positions (lower panels) of the stars that entered the analysis. In particular, we colour-code the positions of the stars according to the radial (panel 6(a)) and vertical (panel 6(b)) force residuals scaled by a typical force, i.e., we show $\Delta F_R(*_i)$ and $\Delta F_z(*_i)$ in Equations (28)-(29). The overplotted grey contours correspond to $\Sigma_{1.5\text{kpc},\text{disk,T}}/\Sigma_{1.5\text{kpc},\text{disk,S}} = 1.15$, i.e., the true vs. the symmetric disk surface density, and mark the position of the spiral arms. The red dots mark stars for which the best fit model underestimates the (absolute value of the) force. This is the case for the radial force in the leading sides of the spiral arms and the vertical force within the spiral arms, which cannot be reproduced. Blue marks correspondingly stars for which the force is overestimated. Overall the radial forces are very well recovered, which is related to the good recovery of the circular velocity curve in Figure 5(a). There are more problems with the vertical force, which is related to the higher surface densities in spiral arms which slightly biases the overall *RoadMapping* model. [TO DO: Might be, that I have to re-calculate the forces for some of the stars. Write Test that tests if force < 1e10 and then recalculates those forces.]

simulation snapshot (averaged over the whole $\Delta\phi = 2\pi$) and the axisymmetric reference DEHH-Pot from Table 2 with the best fit MNHH-Pot from the *RoadMapping* analysis. In particular, Figure 4 illustrates the overall matter density distribution, Figure 5 the rotation curve, surface density profile and halo-to-disk ratio and Figure 6 compares the true and recovered (median) gravitational forces at the position of each star in the data set.

The recovery of density, surface density, circular velocity curve and disk-to-halo ratio is especially good in the region where most of the stars are located, around $R \sim 6\text{kpc}$ and in the plane of the disk. In large regions inside the survey volume, and even outside, the density is recovered to within 15%. The circular velocity curve is even recovered to within 5%, which is also approximately the extent of perturbation that the spiral arms cause with respect to a smooth rotation curve.

There is however a very small ($< 1.5\%$) underestimation of v_{circ} at larger radii. We suspect that this is a combination of a bias introduced by the spiral arms (see also discussion in Section 4.2.4) and the choice of potential model (as a similar bias shows up in the DEHH-Pot). The overall surface density profile is a bit overestimated ($\sim 15\%$) at smaller radii; the reason is clearly the local spiral arm at $R \sim 6\text{kpc}$ with its higher surface density and many stars entering the analysis, which bias the result and which was to be expected. At larger radii ($R \sim 10 - 12\text{kpc}$) the fit of radial local density and surface density profile is less good, which we account to the Miyamoto-Nagai disk having a shallower radial profile than an exponential disk, and not enough stars in this outer regions to give good constraints. The much

stronger bias in the disk-to-halo ratio at larger radii is the result of a misjudgement of the halo scale length. As we will see later (in Section 4.2.3 and Figure 11) we seem to need an even larger survey volume to have enough radial coverage to constrain the halo scale length properly. But again, where most of the stars are located, our *RoadMapping* model is a very good average model for the true galaxy.

The aspect of the potential to which the stellar orbits are actually sensitive to, are the gravitational forces. In Figure 6 we compare therefore the true force that each star in the data set feels (i.e., the radial force, $F_{R,T}(*_i)$, and vertical force, $F_{T,M}(*_i)$, calculated as the sum of the individual contributions by each particle in the simulation and the analytic dark matter halo at the position of star $*_i$) with the force that the *RoadMapping* median model predicts for each star ($F_{R,M}(*_i)$ and $F_{z,M}(*_i)$). We scale the difference between truth and model by a typical radial or vertical force at the given radius for which we use

$$F_{R,\text{typ}}(R) \equiv v_{\text{circ},S}^2(R)/R \quad (25)$$

$$F_{z,\text{typ}}(R) \equiv F_{z,S}(R, z = h_z), \quad (26)$$

where $v_{\text{circ},S}$ and $F_{z,S}$ are the circular velocity and vertical force evaluated in the "true symmetric" reference potential DEHH-Pot in Table 2. As typical vertical force at a given radius we use the vertical force evaluated at the scale height $h_z = 0.17\text{kpc}$ of the disk, which is mo-

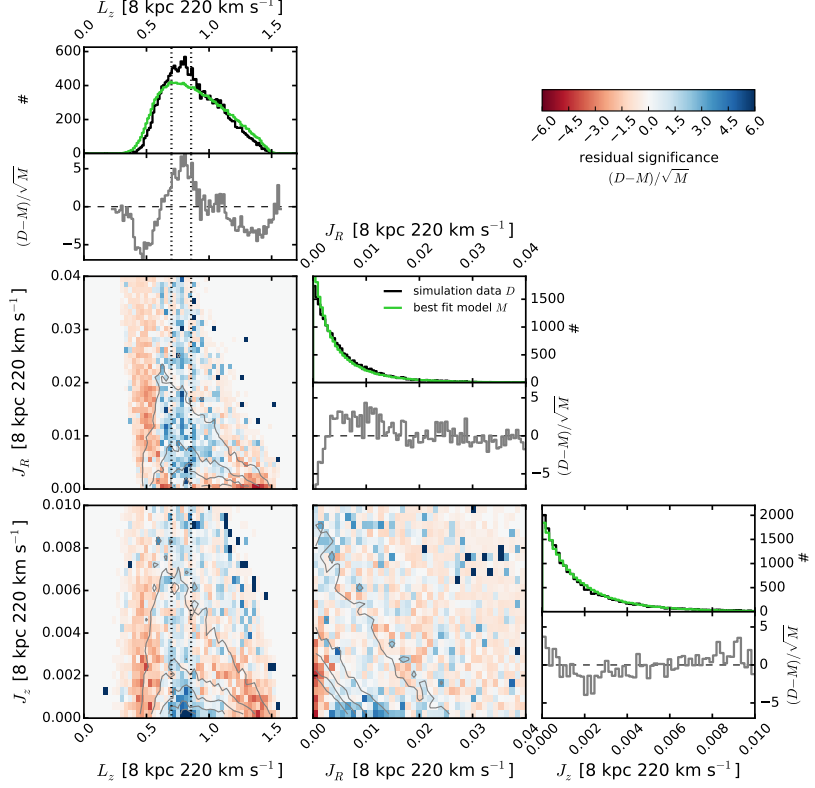


Figure 7. Comparison of the stellar action distribution of the data set D used in the analysis and the recovered axisymmetric action distribution M . (See Figure 3 for the comparison in configuration space.) All actions, of data set and best fit distribution, where calculated in the best fit MNHH-Pot in Table 3. The upper panel in each column shows one-dimensional histograms of the D and M distribution of angular momentum, L_z , the radial action, J_R , and the vertical action, J_z . The other panels display the residual significance $(D - M)/\sqrt{M}$, as both one-dimensional and two-dimensional distribution. (The model M was constructed by MC sampling the best fit qDF, \sqrt{M} is the expected noise due to Poisson statistics, and $(D - M)/\sqrt{M}$ describes therefore how significant any difference between D and M is.) The two-dimensional residuals are over-plotted with equidensity contours of the data D 's two-dimensional action distribution (grey solid lines). In Figure 3(a) we have marked the approximate radial extent of the stronger spiral arm with black dotted lines ($R_{\text{spiral}} \in [5.6, 6.8]$ kpc); the dotted lines in the L_z distributions in this figure correspond to $L_z = R_{\text{spiral}} \times v_{\text{circ}}(R_{\text{spiral}})$. This comparison gives a first impression of how the approximate action distribution in spiral arms might look like. [TO DO: Redo this plot with the new reference data set.] [TO DO: Add in legend that simulation data was calculated in best fit potential too.]

tivated by our findings that

$$\begin{aligned} & \langle |F_{z,S}(*_i)| \rangle(R) \\ & \lesssim \langle |F_{z,T}(*_i)| \rangle(R) \\ & \lesssim F_{z,S}(R, z = h_z) \\ & \lesssim \langle J_z(*_i) \times \Omega_z(*_i) / h_r \rangle(R), \end{aligned} \quad (27)$$

where, e.g., $\langle |F_{z,T}(*_i)| \rangle(R)$ denotes the mean of the absolute value of the true vertical force of all stars at radius R , and $J_z \times \Omega_z \sim \langle E_z \rangle$ is close to the mean vertical energy of a stellar orbit. Figure 6 shows therefore

$$\Delta F_R(*_i) \equiv \frac{|F_{R,M}(R_i, z_i)| - |F_{R,T}(x_i, y_i, z_i)|}{F_{R,\text{typ}}(R_i)} \quad (28)$$

$$\Delta F_z(*_i) \equiv \frac{|F_{z,M}(R_i, z_i)| - |F_{z,T}(x_i, y_i, z_i)|}{F_{z,\text{typ}}(R_i)} \quad (29)$$

for each star. The recovery is as expected: The true vertical force is stronger in the spiral arms (due to the higher surface density) and weaker in the inter-arm regions as compared to the axisymmetric best fit model. The radial force is well recovered where the majority of the stars are located, i.e., in the wide inter-arm regions and in the peaks of the spiral arms. Misjudgments hap-

pen in the wings of the spiral arms: The true radial force (i.e., the pull towards the galactic center) is stronger at the outer edge/leading side of the spiral arm because of the additional gravitational pull towards the massive spiral arm, and for the same reason weaker at the inner edge/trailing side. Overall the recovered *RoadMapping* model appears to be a good mean model, averaging over spiral arms and inter-arm regions.

4.1.3. Recovering the action distribution

In Sections 4.1.1 and 4.1.2 we have demonstrated the goodness of the fit in the configuration space of the data, and of the recovered gravitational potential. What *RoadMapping* is actually fitting is however the distribution in action space. Figure 7 compares the data and the model action distribution (generated by the best fit qDF) given the best fit MNHH-Pot in Table 3. (We use this axisymmetric potential to calculate the actions which lead to the best fit model, and do not attempt to estimate the true actions in the true potential.)

We note that the radial and vertical action distribution fits indeed quite well; the axisymmetric model however contains much more stars on close to circular orbits ($J_R \sim 0, J_z \sim 0$) than the simulation. In the data set

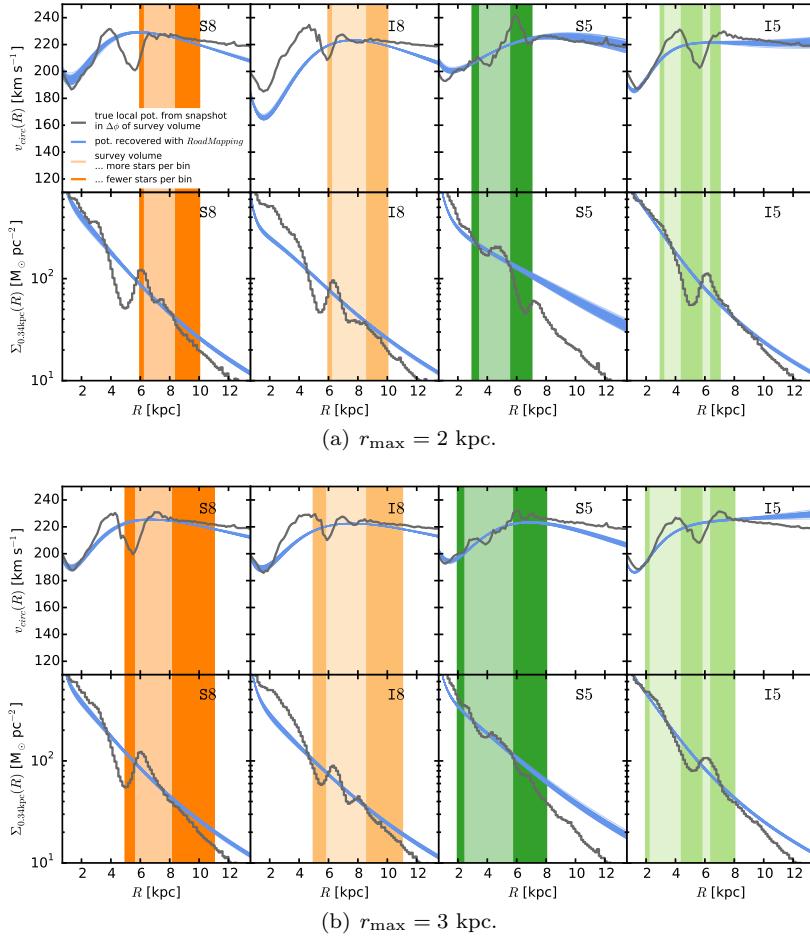


Figure 8. Comparison of the true local circular velocity curve and surface density within $|z| \leq 2 \times h_z = 0.34$ kpc with the recovered *RoadMapping* models from survey volumes of size $r_{\max} = 2$ kpc and $r_{\max} = 3$ kpc. The blue lines show the *RoadMapping* potential models recovered from these data sets (each 100 potential drawn from the full *pdf* sampled with the MCMC). The grey curves show the true profiles as derived from the galaxy simulation snapshot, averaged over the angular wedge $\phi_0 \pm \arcsin(r_{\max}/R_0)$ that encloses the corresponding survey volume (see Table 1 for all R_0 and ϕ_0 values). In other words, we show the true profiles only for the region of the spiral galaxy that was actually probed by the data. The orange and green coloured regions mark the radial extent of the survey volume. We sorted the stars of each data set into radial bins of size $\Delta R = 200$ kpc. The radial bins with a higher than average number of stars are marked with a lighter shade of the corresponding color, and the bins with a lower than average number with a darker shade. It turns out that the constraints of highest accuracy and precision are always where most of the stars are located—within the survey volume and in particular at the peak of the distribution. [TO DO: On y-axis of surface density plots write $\Sigma_{0.34 \text{ kpc}}(R)$] [TO DO: Larger labels]

there is an excess of stars in the galactic plane ($J_z \sim 0$) that have more eccentric orbits than the axisymmetric model would predict. In Figure 3(a) we have marked the radial extent of the stronger spiral arm with dotted lines ($R_{\text{spiral}} \in [5.6, 6.8]$ kpc), and over-plotted the corresponding angular momenta $L_z = R_{\text{spiral}} \times v_{\text{circ}}(R_{\text{spiral}})$ in Figure 7 as a rough estimate where in action space we expect the stars of this spiral arm. It is again obvious that this spiral arm contains (i) more stars in general and (ii) more stars with eccentric orbits ($J_R > 0$) which are (iii) located mostly close to the plane ($J_z \sim 0$), as compared to the axisymmetric model. All of this confirms our expectations for orbits in a spiral arm.

One of the open tasks that the Galactic dynamical modelling community faces, is the description of the orbit distribution of spiral arms. The above exercise of comparing the data and the model actions in a best-fit axisymmetric potential should therefore be performed for any future application to data in the Milky Way as well. It could help to learn more about the approximate orbits that stars move on in real spiral arms, and how spiral

arms perturb axisymmetric action DFs.

[TO DO: Jo writes: "If you make the equivalent of Figure 7 for fits that are especially good and those that are especially bad, is the difference between the qDF prediction and the data that went into the analysis very different? If so, that might be nice to point out and then say that we will investigate this in later work."]

4.2. The influence of spiral arms in *RoadMapping* modelling

In the previous section we showed that for a large survey volume ($r_{\max} = 4$ kpc) *RoadMapping* can construct a good average axisymmetric potential (and DF) model for a galaxy with spiral arms. In the following we want to investigate how this modelling success depends on the position and the size of the survey volume within the galaxy and with respect to the spiral arms.

4.2.1. A suite of data sets drawn from and from between spiral arms

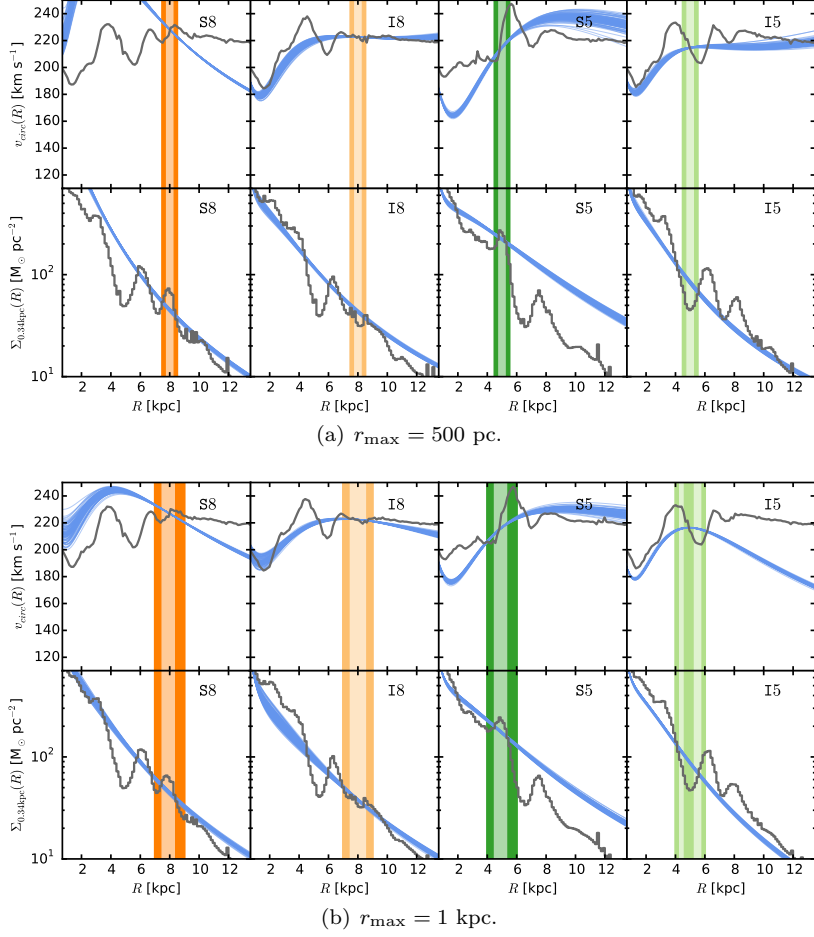


Figure 9. Same as Figure 8, but for all small survey volumes with $r_{\max} = 500$ pc and $r_{\max} = 1$ kpc. [TO DO: On y-axis of surface density plots write $\Sigma_{0.34 \text{ kpc}}(R)$] [TO DO: Larger labels]

To investigate a range of data sets affected in different proportion by spiral arms, we center our test survey volumes at the positions marked in Figures 1 and 2 (see also Table 1) and consider volume sizes with $r_{\max} \in [0.5, 1, 2, 3, 4, 5]$ kpc for $R_0 = 8$ kpc and $r_{\max} \in [0.5, 1, 2, 3, 4]$ kpc for $R_0 = 5$ kpc (to avoid the galactic center). As demonstrated in Figure 2 the spiral arm strength is very different in these test volumes. Each data set that we draw from the simulation contains a random selection of $N_* = 20,000$ stars inside the given spherical volume and we fit a single qDF and MNHH-Pot to it.

4.2.2. Illustrating RoadMapping's success in recovering the circular velocity curves and surface density profiles

It turns out that RoadMapping was successful in finding reasonable and even very good best fit potential models for each single one of the 22 test data sets independent of size and location—given the data and limitations of the model. To illustrate this and to make this encouraging result immediately obvious, we explicitly show the circular velocity curves and surface density profiles of all analyses in Figures 8-10.

In contrast to Figure 5, these Figures only show the true profiles for the region within the galaxy where the data comes from: averaged over the angular wedge covering the radial extent of the survey volume, $\Delta\phi =$

$\phi_0 \pm \arcsin(r_{\max}/R_0)$, and within $|z| \leq 2 \cdot h_z = 0.34$ kpc, i.e., twice the scale height of the disk, which contains most of the disk mass. This is the matter distribution in which the stars are currently moving, and therefore the potential to which the modelling should be sensitive to. In Figures 8-10 we also mark the survey volume and the radial bins of size $\Delta R = 200$ pc with the highest number of stars.

Even though the curves vary extremely between the individual data sets, it becomes very obvious that it is indeed the regions in which the majority of stars is located that drives the RoadMapping fit. And that, no matter if this region is dominated by a spiral arm or inter-arm region and no matter if this region is only as small as $r_{\max} = 500$ kpc, RoadMapping is indeed constraining the local potential where most of the stars of the data set are located. Also, the constraints are not only most accurate but also most precise in these regions.

Only in the two volumes with $r_{\max} = [0.5, 1]$ kpc at position S8 RoadMapping has some difficulties fitting the circular velocity curve; the model expects a flat or falling rotation curve and is presented with a steeply rising rotation curve due to the spiral arm dominating the region. But given RoadMapping recovers a good average surface density profile and the circular velocity at least at the center of the small volume, the fit is still quite successful.

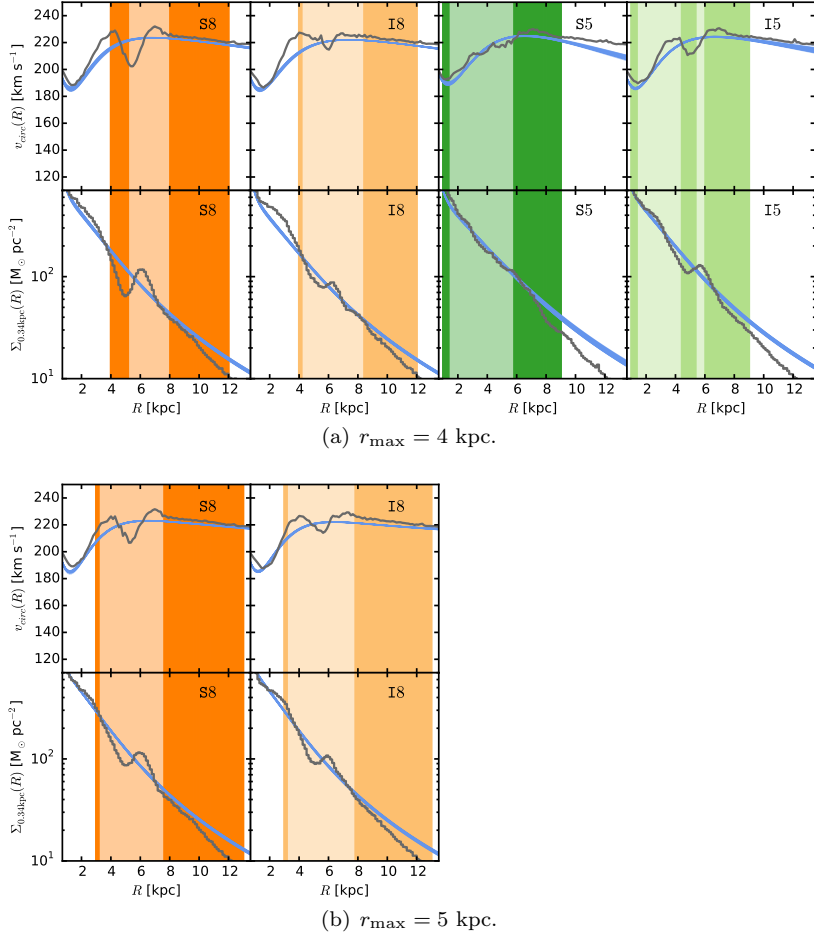


Figure 10. Same as Figure 8, but for all big survey volumes with $r_{\max} = 4 \text{ kpc}$ and $r_{\max} = 5 \text{ kpc}$. [TO DO: On y-axis of surface density plots write $\Sigma_{0.34 \text{ kpc}}(R)$] [TO DO: Larger labels]

In an application to real data in the MW we would also have the possibility to impose some informative prior information on the potential shape (e.g., on the rotation curve), to avoid very unrealistic results (see also discussion in Section 5.4).

[TO DO: Jo writes: "It would be interesting to figure out a little more how we can determine whether we expect the fit to be strongly biased because we are using a volume that it sitting right on top of a massive spiral arm, although that is perhaps best kept for a later paper."]

4.2.3. Discussion of the model parameter recovery

After illustrating in Section 4.2.2 that the potential recovery is qualitatively successful, we will investigate this result more quantitatively in the following two sections. We start here by discussing the recovered best fit potential and qDF parameters for all analyses, which are displayed in Figure 11, and compared to the parameters of the reference DEHH-Pot from Table 2.

Overall the statistical random errors on the parameter recovery are very small for $N^* = 20,000$ and possible systematic errors dominate. There are only a few exceptions ($r_{\max} = 500 \text{ pc}$, $r_{\max} = 1 \text{ kpc}$ at I5, $r_{\max} = 2 \text{ kpc}$ at I8), which we will discuss later.

We will first consider the parameters of the gravitational potential: All volumes recover $v_{\text{circ}}(R_{\odot})$ within a

few km s^{-1} ; in the largest volumes, where the circular velocity curve is probed over several kpc the estimate is the most accurate. The halo fraction f_{halo} of the radial force at the Sun is very well recovered, especially for $r_{\max} \gtrsim 2 \text{ kpc}$. The estimate that we get for the best fit Miyamoto-Nagai disk scale height b_{disk} seems to be also approximately independent of the size of the volume. We can even recover the true halo scale length a_{disk} , however only for a volume as large as $r_{\max} = 5 \text{kpc}$. The models at $r_{\max} = 500 \text{ kpc}$ appear to be too small to constrain the halo at all, and the MCMCs diverged completely for this parameter. Smaller volumes that underestimate a_{halo} get slightly larger estimates for the disk scale length a_{disk} and the overall radial density slope is then probably closer to the truth, even if the individual parameters are not. Outliers can be often explained by having a look at the data: The large disk scale length recovered from the $r_{\max} = 2 \text{ kpc}$ volume at S5 for example mirrors the comparably flat matter distribution caused by two spiral arms close together and dominating the volume (see Figure 8(a) and the large $\sigma_{\Delta \text{Spiral}}$ for this analysis in Figure 2(d)).

The right column of Figure 11 compares the recovered qDF parameters for the different survey volumes with the qDF parameters we got from fixing the potential model to the DEHH-Pot and fitting the qDF only in a $r_{\max} = 5 \text{ kpc}$ volume at S8. Even though the qDF

parameters for small volumes are widely different for different positions within the galaxy, they all approach the values recovered with the DEHH-Pot for larger volumes. There seems therefore to be indeed an overall best-fit qDF describing the average tracer distribution in the galaxy's disk. The only difference is in the $h_{\sigma,z}$ parameter, where the models fitting a MNHH-Pot recover a slightly larger value than the models using the known DEHH-Pot. The reason is that the Miyamoto-Nagai disk has a different radial profile than the double exponential-disk (see Figure 4), which leads to a less steep radial decline in the vertical forces, and therefore mean vertical orbital energies $\langle E_z \rangle \sim \nu \times J_z$, and therefore to a slightly longer $h_{\sigma,z}$ scale length. In general, volumes centered on spiral arms have larger velocity dispersion parameters $\sigma_{R,0}$ and $\sigma_{z,0}$ as compared to volumes at the same radius R_0 but centered on an inter-arm region. And the volumes at $R_0 = 5$ kpc with their stronger spiral arms have larger velocity dispersions than those at $R_0 = 8$ kpc—which is what we expect. Most volumes recover similar tracer scale lengths $h_R \sim 2.5 \pm 0.5$ kpc close to the known disk scale length. Only the volumes centered on the inter-arm region at $R_0 = 8$ kpc (position I8) recover much longer h_R . This might be related to the fact, that volumes at I8 are dominated by an especially extended inter-arm region. The volumes at I5 with $r_{\max} = [0.5, 1]$ kpc were not able to constrain the tracer scale length at all because of the unfortunate position between the rising density wings of two strong spiral arms (see Figure 9).

There are a few survey volumes for which the recovered parameters show some peculiarities: The models from volumes with $r_{\max} = 1$ kpc at I5 and $r_{\max} = 2$ kpc at I8 reject the dark matter halo completely, i.e., $f_{\text{halo}} = 0$. The corresponding halo scale lengths a_{halo} are therefore unconstrained⁹, while the corresponding disk scale heights b_{disk} are grossly overestimated to account for the missing contribution of the spherical halo. We have investigated the reason for this fitting result and found, that for the way how the spiral arms affect the circular velocity curve in these volumes, the recovered models with unusual radial profiles are indeed a better description for the data (see Figure 9(b) and 8(a)). Also, while most analyses average the vertical forces radially over the spiral arms (see Figures 6, lower right panel), for these analyses the averaging happens vertically, i.e., at approximately one scale height above the plane where the model's vertical forces are equally good at all radii (in spiral arms and between), while at small and large $|z|$ the model is bad (see also Figure 13(a) in Section 4.2.4). RoadMapping therefore found a good average fit model also for the stars in these volumes.

Overall we find, that if the volume is large enough to average over several spiral arms and inter-arm regions, an unlucky positioning with respect to the spiral arms does not lead to strong biases in the parameter recovery. We stress again that for particularly large volumes, $r_{\max} = 5$ kpc, we were able to recover all model parameters, including the halo scale length a_{halo} .

[TO DO: Make the same diagnostic plots for 1kpc5Void

⁹ For these analyses and the $r_{\max} = 500$ pc analyses the fit could not constrain a_{halo} and the MCMC was diverging. We had to stop the MCMC after some time, so the a_{halo} might in truth be even less constrained than shown in Figure 11.

as for 2kpc8Void and check that my explanation of $\text{halo}=0$ in this text is indeed correct.]

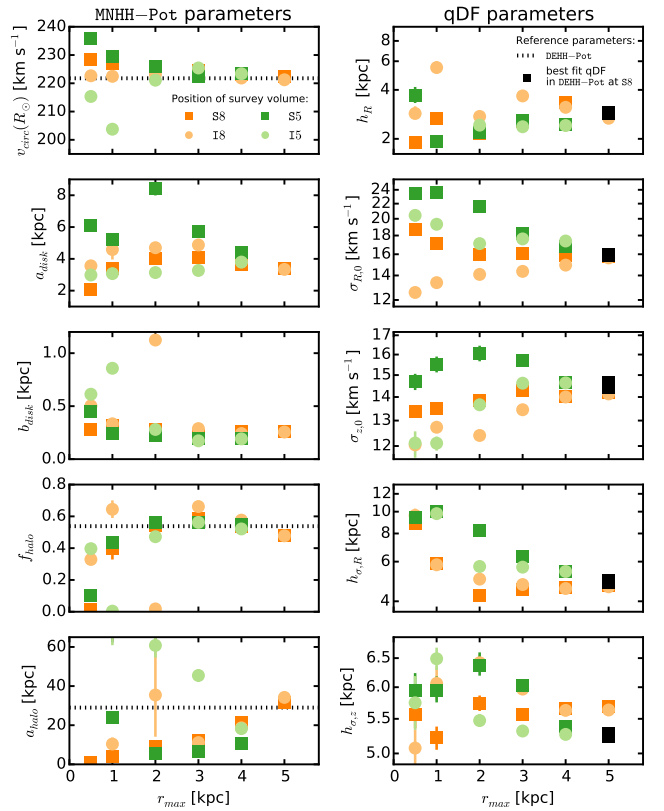


Figure 11. Overview over the model parameter estimates (MNHH-Pot parameters on the left, qDF parameters on the right) recovered with *RoadMapping* from 22 different data sets. All data sets were drawn from the same simulation snapshot, but from survey volumes at different positions in the galaxy (colour-coded) and of different size (r_{\max}) as indicated on the x -axis. Note, that all five qDF parameters are shown here on a logarithmic scale, because *RoadMapping* uses a logarithmically flat prior for them in the fit (see Equation (20)). The black dotted line shows the known model parameters from the reference potential DEHH-Pot in Table 2 (the Miyamoto-Nagai disk parameters a_{disk} and b_{disk} are related but not directly comparable to an exponential disk scale length and height). The black squares denote the qDF parameters we recovered by fixing the potential to the DEHH-Pot, centering a survey volume with $r_{\text{kpc}} = 5$ on the spiral arm at $R = 8$ kpc (position S8), and fitting the qDF only. A survey volume with a radial coverage as large as $r_{\max} = 5$ kpc is required to properly recover all "true" model parameters. [TO DO: Make two plots out of this with sub-captions instead of plot titles.] [TO DO: make max, disk, halo etc. rm mode.]

4.2.4. Success and biases in recovering the gravitational forces

In the previous section we found that the potential and qDF parameters recovered from different survey volumes can be quite different. While the differences can be explained qualitatively, it is not clear yet how good the corresponding potential constraints actually are in a quantitative sense. To test this we calculate again $\Delta F_R(*_i)$ and $\Delta F_z(*_i)$ from Equations (28)-(29) at the position of each star $*_i$ in each data set (see also Figure 6). From the corresponding histograms we derive the median and the 16th and 84th percentiles (1σ range) and show them

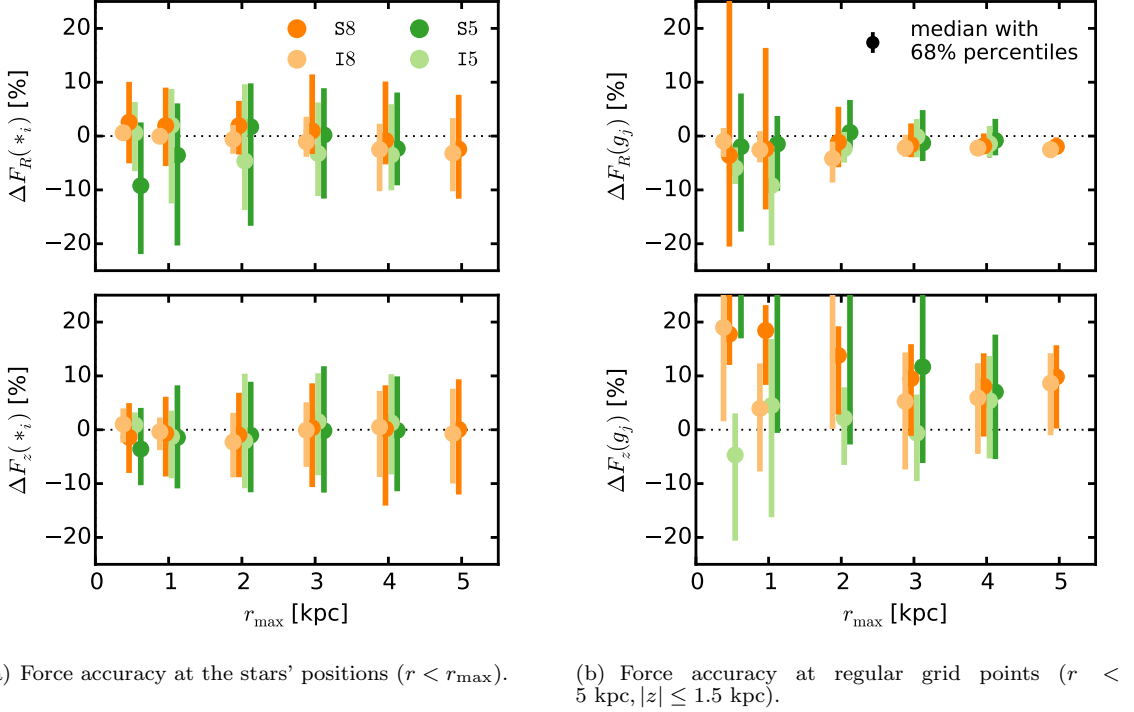


Figure 12. Accuracy of the radial (upper panels) and vertical (lower panels) gravitational forces recovered with *RoadMapping* from the suite of data sets introduced in Section 4.2.1, depending on the size r_{\max} of the survey volume. The left panels investigate how well *RoadMapping* recovers the forces for the ensemble of stars in the data set ($\Delta F_R(*_i)$ and $\Delta F_z(*_i)$ in Equations (28)-(29)) and the right panels test the predictive power of each of the data sets' best-fit potential by showing how well the forces are recovered at regular grid points in a large cylinder of $r_{\max} = 5$ kpc and height $|z| = 1.5$ kpc around the survey volumes center ($\Delta F_R(g_j)$ and $\Delta F_z(g_j)$ in Equations (30)-(31)). For each distribution of $\Delta F(*_i)$ and $\Delta F(g_j)$ we show here the median as dot with the [16th,84th] percentile range as bar. (For presentation purposes we added a small offset $\ll 1$ to r_{\max} on the x -axis.) We find that the forces are very well recovered at the positions of the stars independent of the size of the volume. The spiral arms introduce some biases in the overall recovered potential and we need at least a survey volume of $r_{\max} = 3$ kpc to get a potential with a reasonable predictive power.

in Figure 12(a). We chose this diagnostic because the forces at the positions of the stars are the quantities of the potential to which our modelling is sensitive.

In addition it is interesting to see, how good the extrapolation of a recovered potential describes the overall gravitational potential of the galaxy, i.e., its predictive power. We introduce another diagnostic, that uses a cylindrical grid centred on the respective positions in Table 1, having always a radius of $r_{\max} = 5$ kpc and a height of $z = 1.5$ kpc both above and below the plane. In the (x, y) plane the regular grid points have a distance of 0.25 kpc and in z they have a distance of 0.125 kpc to better sample the thin disk. (We throw out grid points close to the galactic center with $R < 0.125$ kpc, however.) We then evaluate at the position $g_j \equiv (x_j, y_j, z_j)$ of each regular grid point the force residuals

$$\Delta F_R(g_j) \equiv \frac{|F_{R,M}(R_j, z_j)| - |F_{R,T}(x_j, y_j, z_j)|}{F_{R,\text{typ}}(R_j)} \quad (30)$$

$$\Delta F_z(g_j) \equiv \frac{|F_{z,M}(R_j, z_j)| - |F_{z,T}(x_j, y_j, z_j)|}{F_{z,\text{typ}}(R_j)}, \quad (31)$$

analogous to Equations (28)-(29). The two panels in Figure 12(b) show the [16th,84th] percentile range and the median of the grid points' distribution in $\Delta F_R(g_j)$ and $\Delta F_z(g_j)$.

The first and most important thing to learn from Figure 12(a) is, that we get very close to recovering the true

forces at the positions of the stars in the survey volume, no matter how large the survey volume is.

Second, if we consider not the stars inside the survey volume, but the spatial average of the forces in the fixed cylindrical volume ($r_{\max} = 5$ kpc, as described above; Figure 12(b)), the radial forces are overall very well recovered, especially for large survey volumes. There is however an overestimation of $\sim 5 - 20\%$ in the vertical forces (depending on volume size and position) which is induced by the spiral arms (see explanation below).

Third, the constraints we get on the spatially averaged forces inside $r < 5$ kpc are almost as good for the survey volume of $r_{\max} = 3$ kpc as compared to survey volumes of $r_{\max} = 4$ or 5 kpc. If we had to decide between a $r_{\max} = 3$ kpc volume with good data quality and a larger volume with worse data quality, we would loose nothing in terms of predictive power when using the smaller volume. (Only the halo scale length might not be as well constrained, see Figure 11).

What are the reasons for the biases that we observe in Figure 12?

The peak of the distribution in $\Delta F_R(*_i)$ and $\Delta F_R(g_j)$ is slightly biased towards an underestimation of $|F_{R,M}|$ in our *RoadMapping* models. We believe the explanation for this to be the following: Spiral arms are very thin. If a spiral arm crosses the observation volume both its leading side (at large radii) and its trailing side (at small radii) are also in the volume. Stars in the trailing side

feel a lower gravitational pull towards the galaxy center than they would if there was no spiral arm. Because there are in general more stars at smaller radii, the *RoadMapping* fit is slightly biased to reproduce in general slightly weaker radial forces (see also Figures 5 and 6).¹⁰

The peak of $\Delta F_z(*_i)$ is approximately at 0, while the peak of $\Delta F_z(g_j)$ is strongly biased towards an overestimation of $|F_{z,M}|$. There are much more stars in the spiral arms than in the inter-arm regions, and the stars in the spiral arm feel stronger vertical forces because of the higher disk mass. *RoadMapping* finds a model that in general has much stronger vertical forces than expected for a smooth potential. While the actual vertical forces that the many stars in the spiral arms feel are very well recovered, it becomes obvious when looking at the grid points regularly distributed in space, that the *RoadMapping* vertical forces are too strong on a spatial average. We illustrate this also in Figure 13: Regions far away from the strongest spiral arms (at large R and large $|z|$, see Figure 1) are not well described by a potential derived mostly from stars in spiral arms. As expected the overestimation of $|F_{z,T}(g_j)|$ in Figure 12(b) is especially strong ($\sim 20\%$) for small survey volumes dominated by spiral arms, while small volumes dominated by an inter-arm region result in much better estimates for the spatially averaged $F_z(g_j)$ ($\sim 5\%$ bias). Large volumes lie somewhere in between (bias of $\sim 10\%$).

The stellar number asymmetry in the trailing vs. leading sides of spiral arms is much smaller than the stellar number asymmetry in spiral arm vs. inter-arm region. The bias is therefore visible in the distribution of $\Delta F_R(*_i)$ (because the F_R recovery is biased only by a few stars which leads to a bias which is visible for the majority of stars) and not in $\Delta F_z(*_i)$ (because the majority of stars biases the fit and we therefore recover F_z also for the majority of stars). The bias becomes really pronounced for $\Delta F_z(g_j)$ (because the inter-arm regions dominate when averaging spatially which leads to a large average overestimation of F_z) and stays small for $\Delta F_R(g_j)$ (because trailing and leading sides of spiral arms are similarly important when averaging spatially so it becomes visible that the bias is actually not that big).

4.2.5. The influence of the spiral arm strength on the recovery of the gravitational forces

Figure 12 in Section 4.2.4 gave an overview of how accurate we recover the gravitational forces for our whole suite of data sets (depending on the size of the survey volume). In this figure were also some subtle clues hidden, that the quality of the force recovery could be correlated with the position of the data set with respect to the spiral arms. In the following we will investigate this further.

We proceed by relating the same quantities, i.e., local force recovery at the positions of the stars that entered the analysis and power of a recovered model to predict the forces in a fixed large volume, to the actual strength and dominance of spiral arms in the respective survey volumes (see Section 2.4). In Figure 14 we find a connection between the local force recovery and the relative

¹⁰ In the special case that the survey volume coincidentally only contains part of a spiral arm—as was the case with the analyses for $r_{\max} = [0.5, 1]$ kpc at position I5 (see Figure 9, right panels)—the fitting behaves differently anyway, as was already discussed in Section 4.2.3.

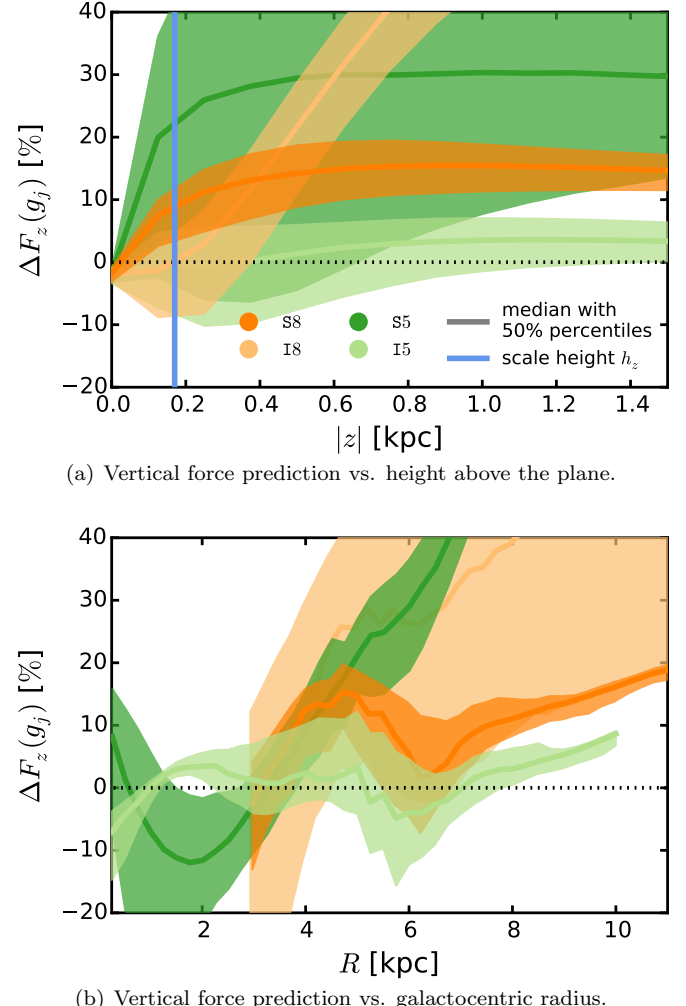


Figure 13. *RoadMapping*'s ability to predict the vertical gravitational force as a function of the height above the plane, $|z|$, and galactocentric radius, R . In particular, we show the predictive power, calculated from Equation (31), for the *RoadMapping* potential models derived from the four data sets with $r_{\max} = 2$ kpc at positions S8, I8, S5, and I5 (colour-coded; see also Figure 1). The coloured bands show the distribution (median with 50% percentiles) of ΔF_z 's of all regular grid points g_j at a given $|z|$ or R . This figure demonstrates the origin of the strong bias in the vertical force prediction, which we found in Figure 12(b). As the fit is driven by the excess of stars that feel stronger vertical forces in the spiral arms, e.g., at $R \sim 3$ kpc or $R \sim 6$ kpc, we get the vertical force right at these radii in the plane of the disk. We consequently overestimate it in the smooth outer regions of the galaxy and at large heights above the plane, where the spiral arms don't play a role. (The potential model with $r_{\max} = 2$ kpc at I8, light orange, is a special case, that was discussed in Section 4.2.3.)

spiral contrast, and Figure 15 shows a trend that the predictive power of the recovered model depends on the dominance of a spiral arm in the survey volume and is better for volumes centred on inter-arm regions.

First, we will take a closer look at Figure 14. Here, we relate $\Delta F_R(*_i)$ and $\Delta F_z(*_i)$ (Equations (28)-(29); see also Figure 12(a)) to the spiral contrast $\sigma_{\Delta\text{Spiral}} \equiv \sigma[\Delta_{\text{Spiral}}(r \leq r_{\max})]$ (Equation (6); see also Figure 2(d)). The average fraction of stars for which the recovery of radial or vertical force is bad (i.e., larger than 10%) decreases with decreasing spiral contrast $\sigma_{\Delta\text{Spiral}}$. This is as expected: Volumes, in which the steep gradient in sur-

face density around a strong spiral arm ($\Delta_{\text{Spiral},k} \neq 0$) is not balanced by larger areas with less perturbations ($\Delta_{\text{Spiral},k} \sim 0$), have (i) a large relative spiral contrast $\sigma_{\Delta\text{Spiral}}$, and (ii) a large relative number of stars affected by the non-axisymmetric kinematics of the spiral arms. And for these stars, the axisymmetric *RoadMapping* model cannot properly predict the forces.

Interestingly, and even though there is some scatter, the force recovery at a given $\sigma_{\Delta\text{Spiral}}$ is on average very similar for the radial and vertical forces (compare the linear fits in Figure 14). This means, that *RoadMapping* attempts to fit both the radial and vertical forces at the positions of the stars, and is not particularly sensitive to just one of them.

As we saw in Figure 2(d), the spiral contrast $\sigma_{\Delta\text{Spiral}}$ increases for the different test volume positions approximately in this order: I8 → S8 → I5 → S5. From Figure 14 follows that this is also the order in which the accuracy of the force recovery decreases. (We did not include this piece of additional information in Figure 14, but it can be seen in Figure 12(a), especially for the smaller volumes.)

Figure 15 stresses even more that the position of the survey volume with respect to the spiral arms matters for the force recovery. Here, we relate the volume averaged predictive power, $\Delta F_R(g_j)$ and $\Delta F_z(g_j)$ (Equations (30)-(31); see also Figure 12(b)) to the dominance of the spiral arm $\langle \Delta_{\text{Spiral}} \rangle$ (Equation (5); see also Figure 2(c)). We show this separately for the volumes centred on spiral arms (S8 and S5; in Panel 15(a)) and the analyses that used data sets drawn from inter-arm regions (I8 and I5; in Panel 15(b)). We derive the fraction of grid points g_j in the reference volume (see Section 4.2.4) with forces that are misjudged by more than 10%, and plot them against $\langle \Delta_{\text{Spiral}} \rangle$ in Panel 15(a), and against $-\langle \Delta_{\text{Spiral}} \rangle$ in Panel 15(b). In that way the x -axis quantifies how much the spiral arms or the inter-arm regions dominate the corresponding survey volume.

Firstly, we note that there is a clear trend that the predictive power gets worse if a spiral arm strongly dominated the survey volume from which the potential constraint was derived. The same trend can be seen for the dominance of inter-arm regions, but it is weaker and less clear.

Secondly, we note that $F_z(g_j)$ is recovered much worse than $F_R(g_j)$. The reason for this was already laid out in Section 4.2.4.

The main result of Figure 15 is however the following: The predictive power of data sets drawn from survey volumes centred on inter-arm regions appears to be in general much better than that of data sets centred on spiral arms. We suspect that the reason for this is, that the stellar distribution between spiral arms is smoother, more extended, and closer to the overall axisymmetric average model, such that the potentials recovered from these volumes have real predictive power for much a much larger volume. This is an important result.

[TO DO: HW writes about the above discussion: "We should discuss this. I am still not 100% sure I get the point. Is the fact that we predict the potential far away from most stars correctly a consequence of having used a clever functional form..?"]

5. DISCUSSION

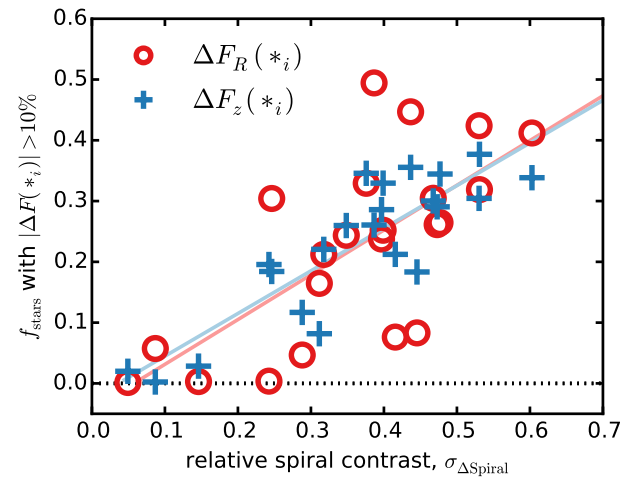


Figure 14. Influence of the spiral arm contrast on the recovery of the gravitational forces at the positions of the stars that entered the *RoadMapping* analysis. Each dot corresponds to one of our 22 data sets. The relative spiral contrast on the x -axis is quantified as $\sigma_{\Delta\text{Spiral}} \equiv \sigma[\Delta_{\text{Spiral}}(r \leq r_{\max})]$ calculated within each survey volume according to Equation (6) in Section 2.4. On the y -axis the fraction of stars (f_{stars}) in each data set is shown for which the radial (red circles) and vertical (blue crosses) force residual calculated from Equations (28)-(29) is larger than 10% (i.e., at 0 all stars have good force measurements, at 1 everything went wrong). The red and blue lines are linear fits to the radial and vertical force residual fraction, respectively, and are guides to the eye that show the clear and expected trend that in volumes with smaller spiral arm contrast, where comparably fewer stars are located in spiral arms, the axisymmetric best-fit model can recover the true gravitational forces also for more stars. On average, the radial and vertical forces are equally well recovered at a given spiral contrast.

5.1. On the informativeness of an orbit distribution function

The qDF is surprisingly informative; even though there was absolutely no indication beforehand that the qDF would be actually a good model for the simulation snapshot; and even though small survey volumes dominated by non-axisymmetric spiral arms are definitely not well-described by the qDF [TO DO: HW writes: "How do we know? Have we shown that?"]. It appears however that a potential model that does not fit the gravitational forces acting on the stars must lead to such an unrealistic orbit/action distribution, that a fit with even such a simple orbit DF as the the qDF is impossible. This demonstrates once more how powerful the concept of an orbit DF is.

[TO DO: Jo writes: "I don't find this so surprising since the N-body simulation is essentially a mono-age population. Perhaps describe more how the stellar disk was setup in the simulation?"]

5.2. On the restrictiveness of the parametrized potential model

We do, on the one hand, use a bulge and halo model that reproduce the true bulge and halo better than we can hope to use one in reality for the MW. The fact that for all except of the largest volumes the true halo scale length is not remotely recovered (and some small volumes even have $f_{\text{halo}} = 0$), and that the contribution of the bulge to the overall potential is small (i.e., the bulge contribution to the total radial force at $R = 8$ kpc

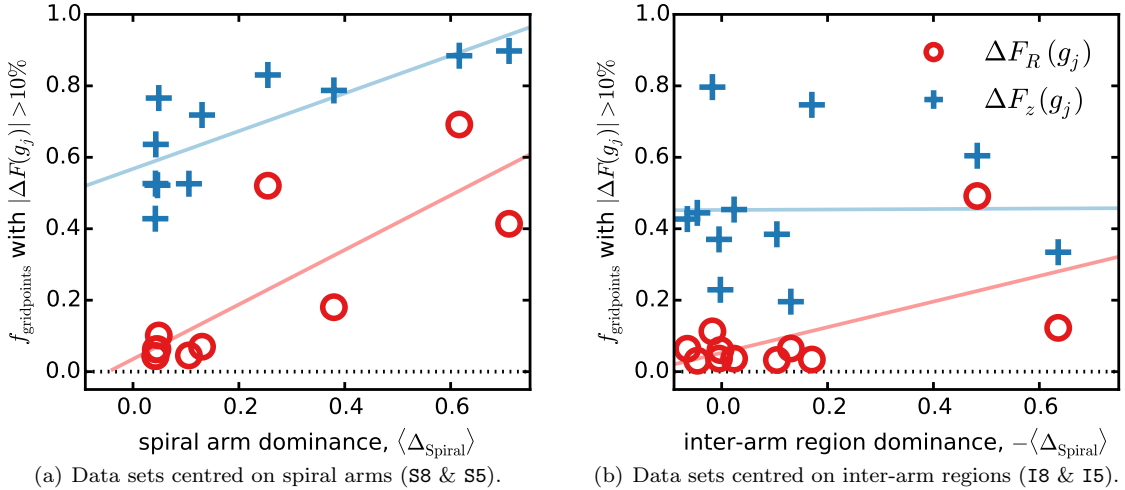


Figure 15. Influence of the spiral arm dominance on the predictive power of the *RoadMapping* potential models recovered from each survey volume. Each point corresponds to one of our 22 *RoadMapping* analyses. How much a spiral arm dominates within a given survey volume is shown on the x -axis of Panel 15(a) and is quantified as $\langle \Delta_{\text{Spiral}} \rangle \equiv \langle \Delta_{\text{Spiral}}(r \leq r_{\max}) \rangle$ from Equation (5) in Section 2.4. In Panel 15(b) we plot $-\langle \Delta_{\text{Spiral}} \rangle$ on the x -axis, which then describes how much an inter-arm region dominates the survey volume. Correspondingly, we show only the data sets centred on spiral arms in Panel 15(a), and those centred on inter-arm regions in Panel 15(b). (At $\langle \Delta_{\text{Spiral}} \rangle = 0$ spiral arms and inter-arm regions average each other out within the survey volume.) The y -axis shows the fraction of a large and fixed cylindrical volume with $r_{\max} = 5$ kpc and $|z| \leq 1.5$ kpc centred around the respective survey volume positions given in Table 1 (i.e., fraction of regular grid points $f_{\text{grid points}}$) with radial (red circles) and vertical (blue crosses) force residuals larger than 10%. This quantifies how well the model can predict the potential in a large portion of the galaxy and at 0 the predictive power is best. The red and blue lines are linear fits and only serve as guide to the eye. This figure demonstrates that the predictive power of a model gets better the less a spiral arm dominates the data set. For the dominance of inter-arm regions this trend is less pronounced. Overall, the radial force can be much better predicted than the vertical force, and survey volumes centred on inter-arm regions have a much better predictive power than those centred on spiral arms.

is only $\sim 9 - 10\%$) remedies this apparent advantage.

We use on the other hand a disk model, the Miyamoto-Nagai disk, that we chose purely for its convenient parametric form and of which we know that it is not a good model for the simulation snapshot, especially not for the radial density profile. As we saw in most figures in this work this might lead to biases in predicting the potential at radii where we have only a few or no stars. But because the spiral arms are such strong perturbations in the overall potential, a better disk model would not give much better results.

It appears that a potential model with a reasonable shape and flexibility (here: disk+bulge+halo structure with 5 free parameters) can do well enough in finding a good fit, both locally for small volumes and overall for large volumes.

5.3. Precision of Gaia measurement errors

Considering measurement uncertainties of distances and proper motions, we found in Paper I that for a survey volume with $r_{\max} = 3$ kpc, distance uncertainties of $< 10\%$ and proper motion uncertainties of [TO DO] *RoadMapping* still gives unbiased parameter results. Even if the proper motion errors are not perfectly known.

At a distance of 3 kpc the measurement uncertainties of bright stars in Gaia lie even below these limits.

In paper I we focussed on recovering completely unbiased model parameters and found that *RoadMapping* is robust to moderate deviations of the model assumptions. In this work we released the condition that the model parameters itself had to be recovered accurately, but allowed *RoadMapping* to simply find an overall best fit for the data strongly affected by spiral arms—which was surprisingly successful in recovering the local poten-

tial even if the model parameters were not recovered.

We therefore presume that in reality we probably have an even larger margin of error before the measurement uncertainties mess up the constraints noticeably than we found in Paper I. And Gaia uncertainties are already below our formal error.

In addition, we found in this work that a volume of $r_{\max} = 3$ kpc should be already big enough to find an overall best fit axisymmetric model for the Galaxy. At larger distances dust starts affecting the measurements. And inside of $R = 3 - 4$ kpc the stellar motions become increasingly non-axisymmetric, possibly because of the Galactic bar (Reid et al. 2014) [TO DO: Jo writes: "Bovy et al. 2015 (and others, see intro)".]

Overall we should therefore be very well off by applying *RoadMapping* to Gaia data within $r_{\max} = 3$ kpc only.

5.4. Location of the Sun in the Milky Way

[TO DO: Jo writes: "Perhaps section 5.4 could be quite a bit shorter, because it is quite speculative and seems oddly detailed given that it's speculative."]

[TO DO: HW writes: "This section seems very long/lengthy to me."]

The Sun is located in one of the smaller spiral arms of the MW, the local Orion spur/arm (Morgan et al. 1953). The Orion arm has long been considered a minor arm within the MW (Blaauw 1985). Two of the MW's major spiral arms pass by the Sun within a few kpc: The Perseus arm is ~ 2 kpc from the Sun (towards the outer MW) (Xu et al. 2006), and the Sagittarius arm at ~ 1 kpc (Sato et al. 2010).

Although, recent observations of stronger star formation (SF) in the Orion arm (Xu et al. 2013) and lower SF in the Perseus arm (Zhang et al. 2013) suggest that

the designation which arms in the MW are "major arms" could be slightly different than previously thought.

The Gaia DR1 in September 2016 will have parallax measurements better than 10% within a maximum range of ~ 500 pc from the Sun (Michalik et al. 2015) [TO DO: I actually calculate that red clump stars have a parallax error of 16% at a distance of 500pc...], the Gaia DR2 at the end of 2017 will cover 2 kpc with good parallaxes [TO DO: My only reference for this is HW. Some paper?]. [TO DO: Jo writes: "Some ..., Lindegren paper for TGAS, de Bruijne 2011? for DR2"]

How reliable *RoadMapping* results from the DR1 will be, depends on the strength of the local Orion arm, which will dominate the survey volume. If previous assessments that it is only a weak spiral arm are correct, we can hope to get already pretty reliable measurements for the overall MW potential. If it is a stronger spiral arm, we might run into some difficulties when modelling such a small volume dominated by a spiral arm (see Figure ??).

However, a recent measurement of the MW's rotation curve by Reid et al. (2014) [TO DO: Not the only measurement, Bovy et al. 2012 for example] confirms again that it is flat. We could impose this condition as a prior constraint in *RoadMapping* (or fix the rotation curve slope as Bovy & Rix (2013) did in their *RoadMapping* analysis), which should greatly help *RoadMapping* to find a good model even from a small volume on a strong spiral arm.

In the Gaia DR2 with a coverage of $r_{\max} \sim 2$ kpc we would in addition to the Orion arm also have the Sagittarius and Perseus arms cross the survey volume. *RoadMapping* should do much better with this volume, because it should become easier to average over spiral arms and inter-arm regions if there are several of them.

The scatter and errors of the rotation curve measurements in Figure 4 by Reid et al. (2014) could hide spiral arm signatures as strong as those of the simulated spiral galaxy in this work. It is however more likely that the MW spiral arms are actually weaker than in this simulation: Reid et al. (2014) measured for example that typical peculiar non-circular motions in spiral arms were around 10 km s^{-1} (and around 20 km s^{-1} in the Perseus arm), while Figure 3(c) about the non-axisymmetric velocity distribution in our simulated galaxy suggests an excess of stars with radial velocities around 50 km s^{-1} .

Reid et al. (2014) also found that within $R \sim 4$ kpc the peculiar motions become much bigger, which could be due to the Galactic bar that stirs up the stellar motions in the center. For *RoadMapping* a volume around the Sun of $r_{\max} = 3 - 4$ kpc should however already give good results.

5.5. Interpreting *RoadMapping* results

[TO DO: Write that, unless the volume is really big, one should only use the potential constraints at the position of the stars.]

[TO DO: Jo writes: "Maybe comment, here or later, that this further shows that the procedure of BR13 was good, i.e., constrain F_z at one radius that corresponds to typical radius."]

5.6. Recovering non-axisymmetric structures in the potential from modelling small volumes

As we saw in Section 4.2.2 and the Figures in Appendix ??, *RoadMapping* makes a very good attempt at fitting the local surface density and circular velocity curve also for volumes as small as $r_{\max} = 500$ pc or 1 kpc. The modelling results might not always be informative about global properties of the potential (i.e., the recovered model does not have a halo, a too thick disk or a overall completely wrong rotation curve slope), but it does tell us about the local potential. It for example correctly predicts a higher surface density in survey volumes dominated by spiral arms, or correctly estimates the circular velocity curve at the median radial position of the stars.

Instead of discarding these globally wrong potential models from small volumes we could actually make use of this interesting property of *RoadMapping* modelling. First of all it implies that we can to a certain extent already trust modelling results from the Gaia DR1 with its small spatial coverage—in particular the gravitational forces at the solar position. At later stages, where we have the full Gaia catalogue with its huge survey volume, we could split the data set not only into different MAPs analogous to Bovy & Rix (2013), but also into different spatial bins in the (x, y) plane of the MW and model each of the smaller volumes separately. This approach would probe the local potential only, even when using an axisymmetric potential model, and should be sensitive to the spiral arms. In this way it should be possible to build up a non-axisymmetric map of the MW potential—with very large spatial pixels however—with constraints from dynamical modelling only. It would be in particular interesting to compare and correlate these results from action-based dynamical modelling with results from dynamical Jeans models of the MW disk, stellar number counts and gas disk measurements to also learn more about the non-axisymmetric distribution of dark matter in the MW disk. [TO DO: Jo writes: "not clear how this would work?"]

6. CONCLUSION

RoadMapping is an axisymmetric dynamical modelling machinery that simultaneously fits an action-based DF and gravitational potential to the individual 6D phase-space coordinates of stellar populations in the MW disk and builds on previous work by Binney & McMillan (2011); Binney (2012); Bovy (2015). *RoadMapping* was first applied by Bovy & Rix (2013); it was improved and tested in detail against the breakdowns of its modelling assumptions by Trick et al. (2016).

In this paper we investigated the robustness of *RoadMapping* when modelling a non-axisymmetric system. We explore this for the first time explicitly by modelling a simulated spiral galaxy by D'Onghia et al. (2013), which has stronger spiral arms than we expect in the MW, and by comparing the results to the true potential. We find that *RoadMapping*-like action-based dynamical modelling is very robust against perturbations of spiral arms, especially if the survey volume is large enough to encompass both spirals and inter-arm regions. In Section 4.1 we demonstrated this in detail for a single *RoadMapping* analysis of a data set with a spatial coverage of radius $r_{\max} = 4$ kpc around a position equivalent to that of the Sun.

We have investigated the role of survey volumes in the

simulated galaxy, differing in size and position with respect to the spiral arms and inter-arm regions. We find that the gravitational forces are mostly well recovered at the locations of the stars that entered the analysis. For survey volume sizes $r_{\max} \geq 3$ kpc the recovered potential model becomes already a good average potential model for the whole galaxy. For some position of the survey volume center, e.g., in a smooth and not too depleted inter-arm region, also smaller models can give good overall constraints. If a small volume is dominated by a very strong spiral arm the constraints become less reliable, as expected. The correct dark matter halo scale length was, however, only recovered for a survey volume as large as $r_{\max} = 5$ kpc.

This overall robustness of *RoadMapping* is in particular notable, as the breakdown of the assumption of axisymmetry implies a breakdown of several model assumptions simultaneously: (i) orbital actions are not fully/strictly [TO DO] conserved anymore, [TO DO: Jo writes: "they will only change slightly."], (ii) the true potential is not spanned by the family of model potentials, (iii) the quasi-isothermal DF need not, or will not, describe the orbit distribution within spiral arms. However, the qDF seems to be informative enough to guide the fit to potential shapes that correctly measure the average surface density within $\sim 2 \times$ [TO DO: HW writes: "does that also refer to teh circular velocity? No? Rephrase"] the disk scale height and the circular velocity where most of the stars that entered the analysis are located—even for small volumes with $r_{\max} = 500$ kpc dominated by spiral arms.

All these results suggest [or "imply"] [TO DO] that *RoadMapping* should be well-suited to making new measurements of the MW's gravitational potential with the upcoming Gaia releases. It might work potentially even with the Gaia DR1, that only covers a small region $r_{\max} = 500$ kpc (where the distance errors are small enough), because the local Orion arm, in which the Sun lies, is thought to be only a minor spiral arm in the MW and should not disturb the modelling too much. [TO DO: HW writes about the last paragraph: "Gaia's fundamental contribution to Galactic dynamics (in HWR's view) will come from a) precise and accurate proper motions, b) a calibration of the distance scale for a nearby subsample. It's OK to say: 1kpc volume such as DR1, but not attribute that solely to the distance accuracy."]

REFERENCES

- Binney, J. 2010, MNRAS, 401, 2318
 —. 2012, MNRAS, 426, 1324
 Binney, J., & McMillan, P. 2011, MNRAS, 413, 1889
 Bird, J. C., Kazantzidis, S., Weinberg, D. H., et al. 2013, ApJ, 773, 43
 Blaauw, A. 1985, in IAU Symposium, Vol. 106, The Milky Way Galaxy, ed. H. van Woerden, R. J. Allen, & W. B. Burton, 335–341
- Blitz, L., & Spergel, D. N. 1991, ApJ, 379, 631
 Bovy, J. 2015, ApJS, 216, 29
 Bovy, J., Bird, J. C., García Pérez, A. E., et al. 2015, ApJ, 800, 83
 Bovy, J., & Hogg, D. W. 2010, ApJ, 717, 617
 Bovy, J., Hogg, D. W., & Roweis, S. T. 2009, ApJ, 700, 1794
 Bovy, J., & Rix, H.-W. 2013, ApJ, 779, 115
 Bovy, J., Rix, H.-W., & Hogg, D. W. 2012a, ApJ, 751, 131
 Bovy, J., Rix, H.-W., Hogg, D. W., et al. 2012b, ApJ, 755, 115
 Bovy, J., Rix, H.-W., Liu, C., et al. 2012c, ApJ, 753, 148
 Bovy, J., Rix, H.-W., Schlafly, E. F., et al. 2016, ApJ, 823, 30
 Churchwell, E., Babler, B. L., Meade, M. R., et al. 2009, PASP, 121, 213
 Das, P., & Binney, J. 2016, MNRAS, 460, 1725
 Dehnen, W. 1998, AJ, 115, 2384
 D'Onghia, E., Vogelsberger, M., & Hernquist, L. 2013, ApJ, 766, 34
 Eyer, L., Holl, B., Pourbaix, D., et al. 2013, Central European Astrophysical Bulletin, 37, 115
 Famaey, B., Jorissen, A., Luri, X., et al. 2005, A&A, 430, 165
 Foreman-Mackey, D., Hogg, D. W., Lang, D., & Goodman, J. 2013, PASP, 125, 306
 Georgelin, Y. M., & Georgelin, Y. P. 1976, A&A, 49, 57
 Hammersley, P. L., Garzón, F., Mahoney, T. J., López-Corredoira, M., & Torres, M. A. P. 2000, MNRAS, 317, L45
 Hernquist, L. 1990, ApJ, 356, 359
 Jurić, M., Ivezić, Ž., Brooks, A., et al. 2008, ApJ, 673, 864
 Liszt, H. S., & Burton, W. B. 1980, ApJ, 236, 779
 Martig, M., Minchev, I., & Flynn, C. 2014, MNRAS, 442, 2474
 Martig, M., Fouesneau, M., Rix, H.-W., et al. 2016, MNRAS, 456, 3655
 Michalik, D., Lindegren, L., & Hobbs, D. 2015, A&A, 574, A115
 Minchev, I., Chiappini, C., & Martig, M. 2014, A&A, 572, A92
 Miyamoto, M., & Nagai, R. 1975, PASJ, 27, 533
 Morgan, W. W., Whitford, A. E., & Code, A. D. 1953, ApJ, 118, 318
 Ness, M., Hogg, D. W., Rix, H.-W., et al. 2016, ApJ, 823, 114
 Newberg, H. J., Yanny, B., Rockosi, C., et al. 2002, ApJ, 569, 245
 Oort, J. H., Kerr, F. J., & Westerhout, G. 1958, MNRAS, 118, 379
 Piffl, T., Binney, J., McMillan, P. J., et al. 2014, MNRAS, 445, 3133
 Reid, M. J., Menten, K. M., Brunthaler, A., et al. 2014, ApJ, 783, 130
 Rix, H.-W., & Bovy, J. 2013, A&A Rev., 21, 61
 Sanders, J. L., & Binney, J. 2015, MNRAS, 449, 3479
 —. 2016, MNRAS, 457, 2107
 Sato, M., Hirota, T., Reid, M. J., et al. 2010, PASJ, 62, 287
 Springel, V., Di Matteo, T., & Hernquist, L. 2005, MNRAS, 361, 776
 Ting, Y.-S., Rix, H.-W., Bovy, J., & van de Ven, G. 2013, MNRAS, 434, 652
 Trick, W. H., Bovy, J., & Rix, H.-W. 2016, ArXiv e-prints, arXiv:1605.08601
 Vera-Ciro, C., & D'Onghia, E. 2016, ApJ, 824, 39
 Wegg, C., & Gerhard, O. 2013, MNRAS, 435, 1874
 Williams, M. E. K., Steinmetz, M., Binney, J., et al. 2013, MNRAS, 436, 101
 Xu, Y., Newberg, H. J., Carlin, J. L., et al. 2015, ApJ, 801, 105
 Xu, Y., Reid, M. J., Zheng, X. W., & Menten, K. M. 2006, Science, 311, 54
 Xu, Y., Li, J. J., Reid, M. J., et al. 2013, ApJ, 769, 15
 Yanny, B., Rockosi, C., Newberg, H. J., et al. 2009, AJ, 137, 4377
 Zhang, B., Reid, M. J., Menten, K. M., et al. 2013, ApJ, 775, 79